Review Article

Nano Research
2024, 17(3): 1288–1312

ISSN 1998-0124 CN 11-5974/O4
https://doi.org/10.1007/s12274-023-5889-2

Achieving high-performance sodium metal anodes: From structural design to reaction kinetic improvement

Jing Xu[1] (✉), Jianhao Yang[1], Yashuang Qiu[1], Yang Jin[1], Tianyi Wang[2] (✉), Bing Sun[3] (✉), and Guoxiu Wang[3] (✉)

[1] *Research Center of Grid Energy Storage and Battery Application, School of Electrical and Information Engineering, Zhengzhou University, Zhengzhou 450001, China*
[2] *College of Chemistry and Chemical Engineering Yangzhou University, Yangzhou 225009, China*
[3] *Centre for Clean Energy Technology, School of Mathematical and Physical Sciences, Faculty of Science, University of Technology Sydney, Ultimo, NSW 2007, Australia*

Received: 27 April 2023 / **Revised:** 30 May 2023 / **Accepted:** 2 June 2023

ABSTRACT

Sodium metal is one of the ideal anodes for high-performance rechargeable batteries because of its high specific capacity (~ 1166 mAh·g^{-1}), low reduction potential (−2.71 V compared to standard hydrogen electrodes), and low cost. However, the unstable solid electrolyte interphase, uncontrolled dendrite growth, and inevitable volume expansion hinder the practical application of sodium metal anodes. At present, many strategies have been developed to achieve stable sodium metal anodes. Here, we systematically summarize the latest strategies adopted in interface engineering, current collector design, and the emerging methods to improve the reaction kinetics of sodium deposition processes. First, the strategies of constructing protective layers are reviewed, including inorganic, organic, and mixed protective layers through electrolyte additives or pretreatments. Then, the classification of metal-based, carbon-based, and composite porous frames is discussed, including their function in reducing local deposition current density and the effect of introducing sodiophilic sites. Third, the recent progress of alloys, nanoparticles, and single atoms in improving Na deposition kinetics is systematically reviewed. Finally, the future research direction and the prospect of high-performance sodium metal batteries are proposed.

KEYWORDS

sodium metal anodes, interface engineering, current collector design, reaction kinetics, sodium deposition processes

1 Introduction

With the development of consumer electronics, electric vehicles (EVs), and smart grid storage technologies, the demand for high energy-density and low-cost rechargeable batteries continues to grow [1–4]. Rechargeable lithium-ion batteries (LIBs) are currently the most successful commercially developed batteries and occupy a dominant position in the market [5–7]. However, due to the limitation of cathode and graphite anode capacity, LIBs can only reach an energy density of 250 Wh·kg^{-1}, which cannot meet the high energy demand of electric vehicles and next-generation energy storage [8–10]. Due to the high energy densities and low redox potentials, alkali metals, such as lithium (Li), sodium (Na), and potassium (K), have been directly used as anode materials in rechargeable batteries [11]. In terms of material availability, Na possesses a significant advantage over Li and K [12]. Sodium resources can be obtained through different resources, such as hard rock mining, brine, and seawater [13]. Compared with Li (0.0017 wt.%) and K (1.5 wt.%), Na resources are more abundant (2.3 wt.%) in the earth's crust and can be obtained through different resources worldwide [14, 15]. Therefore, Na metal has a significant low-cost advantage over Li and K metal. Meanwhile, Na metal anodes have advantages such as higher theoretical capacity (~ 1166 mAh·g^{-1}), lower redox potential (−2.71 V compared to standard hydrogen electrodes), and high energy density, which make the Na metal batteries can match the requirements of large-scale energy storage systems [16–18].

Despite the huge potential, there are still several key issues and challenges to be solved before the large-scale commercialization of Na metal anodes, as follows: (1) Compared with Li metal, Na metal has much higher reactivity. Most available organic electrolytes can be reduced on the surface of the Na metal anode to form solid electrolyte interphase (SEI). The loose and porous structure makes SEI easily break and produce cracks, continuously consuming the electrolyte by repeated reactions with freshly exposed Na metal; (2) safety problems caused by the growth of Na dendrites. The accumulation of sharp Na dendrites may penetrate the separator and cause internal short circuit. Moreover, these fragile Na dendrites could be isolated from the Na metal anode during the stripping process, leading to the formation of "dead Na" and reducing Na metal utilization; (3) the large volume changes caused during Na plating/stripping. Due to the hostless nature, the volume change of Na metal anode is relatively infinite. The

Address correspondence to Jing Xu, xu.jing@zzu.edu.cn; Tianyi Wang, wangty@yzu.edu.cn; Bing Sun, Bing.Sun@uts.edu.au; Guoxiu Wang, Guoxiu.Wang@uts.edu.au

continuous volume change will generate huge mechanical stress, which will exacerbate the cracks of SEI and further accelerate the growth of Na dendrites. [16, 18–20]. These problems affect each other, resulting in low Coulombic efficiency (CE), poor cycle stability, and short cycle life of Na metal anodes.

In order to solve these problems and realize the commercial application of Na metal anodes, researchers have developed various methods of Na metal protection. The first common strategy is the interface engineering by using electrolyte additives or manual pretreatment to form a strong protective layer on the surface of the Na metal anode to protect it from severe corrosion [21–23]. In lithium metal batteries (LMBs), a variety of electrolyte additives have been used to construct stable SEI layers, such as fluoroethylene carbonate (FEC) and lithium nitrate ($LiNO_3$) [24, 25]. Similarly, many studies have introduced various solvents, salts, and additives into the electrolyte to promote the electrochemical stability of Na metal anodes. $NaPF_6$, FEC, and other fluorine-containing salts and additives may generate a NaF-rich SEI layer *in situ* during the electrochemical process [26]. Another approach is to build an inorganic/organic layer by precoating, such as atomic layer deposition (ALD) technology, which can coat an effective passivation layer to prevent metal corrosion [27, 28]. However, the protective layer cannot withstand the mechanical stress caused by the volume change of Na metal in a long-time cycle, resulting in rupture and loss of protection. The second strategy is the construction of three-dimensional (3D) substrates to reduce the local deposition current density and the volume change [17, 29]. In terms of the host structure designs, the porous 3D current collectors are capable of effectively adapting to the volume expansion of anode. The 3D porous frame with the high specific surface area significantly increases the contact surface between electrode and electrolyte, effectively averages the electric field distribution, and disperses the local current density, thus achieving uniform Na electrodeposition [17, 30–32]. Unfortunately, the relatively large 3D matrix weight inevitably compromises the energy density of batteries. Although carbon-based frames have a relatively light weight, the lack of sodiophilicity of carbon surfaces may impair their ability to regulate uniform plating and effectively load Na metal [19, 33].

More importantly, the electrodeposition process of Na^+ undergoes a series of processes, such as desolvation, nucleation, and diffusion [34, 35]. The large energy barrier leads to the slow Na ions/atoms transport kinetics, which is the major reason to causing random deposition, dendrite growth, and SEI failure [18, 36]. To solve the Na metal anode failure problem, Na uniform deposition behavior needs to be regulated. Improving the sodiophilicity of the anode surface can not only regulate the surface energy to create a thermodynamically favorable environment for Na deposition, but also effectively reduce the nucleation overpotential [37]. In addition, increasing the diffusion rate of Na ions/atoms, both in the SEI film and along the electrode surface, can kinetically ensure that the Na^+ flux is quickly and uniformly distributed to the nucleation site even at high current densities [38]. Therefore, a combination of the two strategies would be an ideal solution to achieve uniform Na deposition. Applying the basic principles of conventional catalysis is an effective way to reduce the energy barrier of chemical reactions. In terms of Li metal batteries, there have been many reports of the use of catalytic means to regulate the behavior of Li plating [39, 40]. In fact, the Na and Li metals are in the same group of alkali metals, so catalyst design principles can also be implemented to accelerate Na nucleation and diffusion kinetics [16]. It should be noted that the affinity of the catalyst for Na should be moderate to avoid the difficulty of Na stripping caused by strong adsorption. Meanwhile, it is important to maintain a balance between the lateral diffusion rate of Na ions/atoms and the vertical local deposition rate. Slow lateral diffusion rate tends to cause dendrite formation and growth, while excessively fast diffusion rates may exacerbate random Na nucleation behavior [41].

Herein, we comprehensively review the progress of Na metal anode protection from physical structure design to diffusion reaction kinetics enhancement. The progress in interface engineering is first summarized and classified according to the components of SEI: inorganic, organic, and inorganic/organic mixtures. Then, the latest reports of 3D current collectors made from metal-based, carbon-based, and composite materials in recent years are summarized. Thirdly, the method of adjusting Na deposition and nucleation by alloy layers, nanoparticles (NPs), and single-atom-catalysts (SACs) is introduced (Fig. 1). Finally, the future research direction of Na metal anodes is prospective.

2 Interface engineering design

The SEI layer plays an important role in Na plating/stripping process, and a stable SEI layer is essential for achieving long-life Na metal anodes [42]. The composition and morphology of the SEI layer directly affect the stability of the cycle [43]. An ideal SEI should have the following characteristics: electrical insulation, high ionic conductivity, high mechanical strength, excellent compactness to prevent solvent penetration, smooth surfaces, and uniform electric field distribution [44]. However, the natural formation of SEI on the surface of Na metal anodes is usually loose and discontinuous, resulting in uneven ion diffusion, further causing Na dendrite formation and other problems [45]. To address these issues, robust SEI layers are often constructed by pretreatment or adjusting the electrolyte composition [13]. According to composition, the SEI layers can be divided into inorganic, organic, and organic/inorganic hybrid layers.

2.1 Inorganic interphase engineering

In the process of Na deposition, Na^+ should pass through the SEI layer to the anode surface to obtain electrons and convert into Na atoms. In general, the diffusion of Na^+ in the SEI membrane is slow, which may cause dendrite growth. Improving the ionic conductivity of the interface layer is an effective way to achieve stable Na metal anodes. High ionic conductivity can effectively promote Na^+ diffusion and reduce interfacial resistance. In addition, the high shear modulus is conducive to inhibiting the continuous growth of dendrites. Therefore, inorganic layers with high shear modulus and high ionic conductivity are widely used in metal anode protection [46–48].

The Na-halide (F/Br/I) protective layers have always been the focus of research for their excellent ability to inhibit Na dendrites. NaF is the most common inorganic component of SEI in Na metal anodes, which has the advantages of high Young's modulus (74.66 GPa) and high interfacial energy (0.045 $eV·Å^{-2}$) [49, 50]. Cui et al. reported for the first time that SEI composed of NaF can effectively inhibit the formation of Na dendrites [51]. They found $NaPF_6$ could form a homogeneous SEI composed of inorganic Na_2O and NaF, which was highly impermeable to electrolyte solvents. Several researchers have reported shown that NaF-rich SEIs could be formed using Na fluoride salts (sodium bis(trifluoromethylsulfonyl)imide (NaTFSI) and sodium bis(fluorosulfonyl)imide (NaFSI)) [52, 53]. Increasing the F content of the electrolyte through the use of fluorine-containing solvents and additives is also an effective strategy. Huang et al. designed a high F-content electrolyte, 1.0 M $NaPF_6$ in FEC/PC/1,1,2,2-tetrafluoroethyl 2,2,3,3-tetrafluoropropyl ether (HFE) + PFMP (PC = propylene carbonate; PFMP = perfluoro-2-methyl-3-pentanone) [54]. The content of F in SEI on Na metal

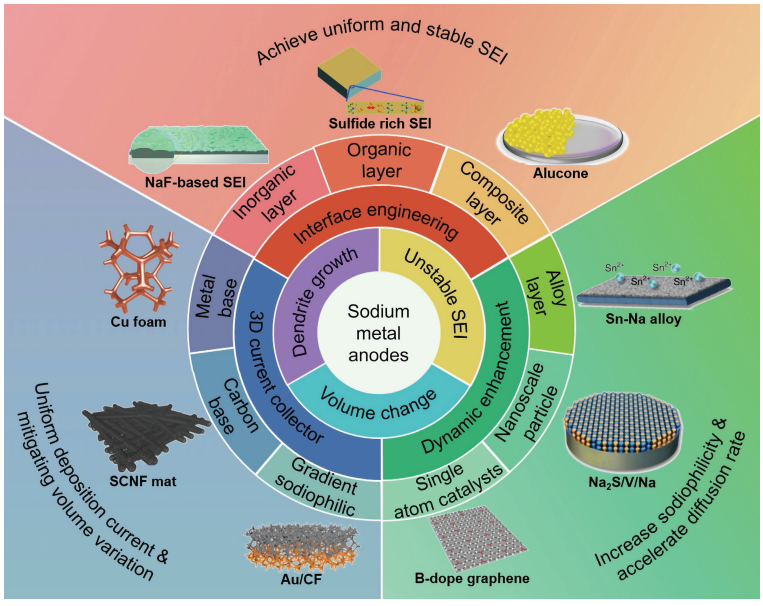

Figure 1 Existing problems and improvement strategies of sodium metal anodes. Reproduced with permission from Ref. [54], © The Royal Society of Chemistry 2020. Reproduced with permission from Ref. [74], © American Chemical Society 2020. Reproduced with permission from Ref. [84], © WILEY-VCH Verlag GmbH & Co. KGaA, Weinheim 2020. Reproduced with permission from Ref. [111], © Elsevier Ltd. 2020. Reproduced with permission from Ref. [125], © Wiley-VCH GmbH 2022. Reproduced with permission from Ref. [136], © Wiley-VCH GmbH 2020. Reproduced with permission from Ref. [159], © Macmillan Publishers Limited, part of Springer Nature 2018. Reproduced with permission from Ref. [168], © Wiley-VCH GmbH 2023. Reproduced with permission from Ref. [182], © WILEY-VCH Verlag GmbH & Co. KGaA, Weinheim 2019.

surface was mainly contributed by FEC (~ 23.5 at.%), which was further increased by adding PFMP (~ 27.2 at.%). However, these methods have several disadvantages, such as high cost, high toxicity, and poor compatibility. It is widely accepted that the inorganic species in SEI are mainly related to the decomposition of anions in the electrolytes. Therefore, it is also a promising method to promote the decomposition of more anions on the surface of the Na metal anode by cationic solvation [55–57]. By adding 4-acetylpyridine (4-APD), Ma's group achieved the anion-enriched solvation structure, which induces the formation of the NaF-rich SEI on the Na anode [58]. The 4-APD additive migrated to the surface of the Na anode with the solvated group. Owing to the high Gibbs free energy difference (ΔG), the 4-APD$^-$ (ΔG_1 = −21.1 kJ·mol^{-1}) preferred to bind with the solvent molecules. Therefore, more PF_6^- (ΔG_2 = −18.6 kJ·mol^{-1}) decomposed into NaF during the formation of SEI. Thus, the SEI with more than 70% of NaF was formed (Fig. 2(a)).

Forsyth et al. investigated the effect of salt concentration and applied electrode potential on the chemical composition of the innermost interfacial layer in ionic liquid (IL) (i.e., C3mpyrFSI) [59]. The [C3mpyr]$^+$/[FSI]$^-$ ratio of neat-IL and low-salt-concentration electrolyte increased with the increase of anode potential applied. In contrast, in the 50 mol% salt system, the ratio decreased from 0.60 to 0.33 as the potential changed from −0.5 to −1.25 V relative to the potential of zero charge (PZC) (Fig. 2(b)), and the number of Na^+ in the innermost layer increases significantly (Fig. 2(c)). The competitive relationship between [C3mpyr]$^+$ and Na^+ resulted that the smaller Na^+ filled the innermost free space more easily than [C3mpyr]$^+$, which led to the reduction of [C3mpyr]$^+$ cations and brought more [FSI]$^-$ anions. High concentration of NaFSI salt and low electrode potential facilitated the binding of Na^+ and [FSI]$^-$ anions to form large molten salt-like $Na_x(FSI)_y$ aggregates, which improved the rate of Na metal nucleation and deposition. In addition, the uniform distribution of [FSI]$^-$ near the anode surface and the expulsion of [C3mpyr]$^+$ from the innermost layer contribute to the formation of a more uniform and homogeneous SEI layer through the decomposition of [FSI]$^-$ into NaF. After Na symmetric cell based on C3mpyrFSI IL with the 50 mol% NaFSI salt was pretreated with negative polarization, the long galvanostatic cycling at 1.0 mA·cm^{-2}/0.1 mAh·cm^{-2} was very stable, without significant failure for more than 700 cycles.

The surface transport barrier of Na^+ is affected by the chemical composition of SEI. By joint density functional theory (JDFT), Archer and coworkers proved that the binding energy of a Na adatom depends on its position on the surface of the Na-halide [60]. For NaF, the lowest energy point of the Na adsorption atom was located at the top of the fluoride-ion, and this site was called the "anion site". The saddle point on the diffusion path was located in the middle of two adjacent anion sites and was called the "in-between site" (Fig. 2(d)). The increase of anion size will make the intermediate site close to the anion site, and the saddle point of NaBr is just the minimum, resulting in the lowest diffusion barrier of ion transport at the interface: only about 0.02 eV per atom. Therefore, the deposition of the ions at the Na interface is less restricted, which could prevent the formation of dendrites. In another work, Wang's group found that NaI also had a much lower diffusion barrier of 0.02 eV for Na adatoms [61]. Excellent Na metal iodine batteries are achieved by *in situ* NaI coating with ultra-stable cycling performance (at 2 C > 2200 cycles), high capacity (210 mAh·g^{-1} at 0.5 C), high discharge voltage platform (> 2.7 V), and low overpotential.

In addition to Na-halides, studies on SEI composed of other inorganic compounds also emerged in recent years. Yu et al. for the first time used a simple method to design an *in situ* SEI composed of Na_3P [62]. By grinding red phosphorus (P) powder repeatedly on the surface of Na metal at room temperature (RT), Na_3P layer was formed on the surface of Na metal. The Na_3P layer has high Young's modulus (8.6 GPa), high ionic conductivity (~ 0.12 mS·cm^{-1}), and low energy barrier (11.0 kJ·mol^{-1}), which results in a more uniform ionic flux and effectively inhibits the dendrite growth. *In situ* optical observations of Na deposition in transparent quartz symmetric cells demonstrated that the Na_3P layer was very effective in stabilizing the interface and inhibiting dendrite growth (Fig. 2(e)).

Inorganic substances have different characteristics and

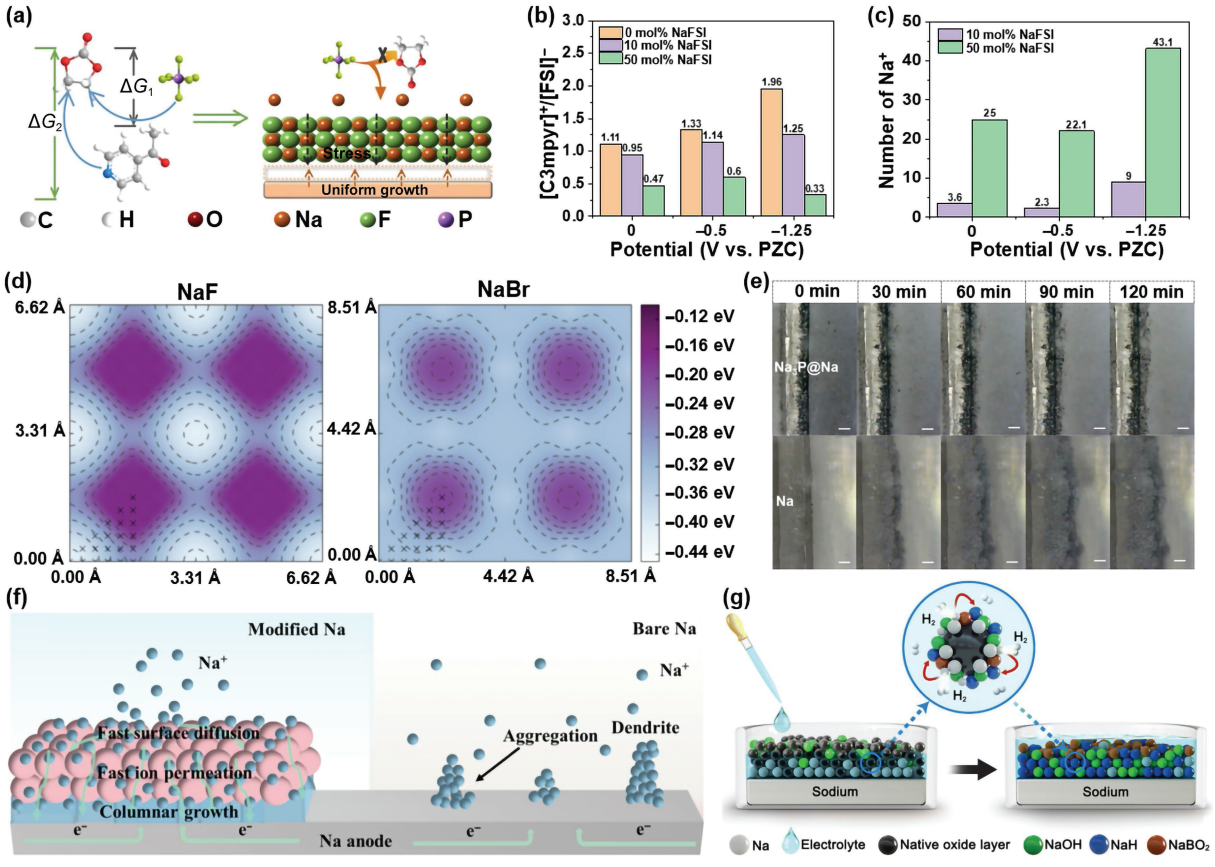

Figure 2 (a) The illustration of the decomposition of PF_6^- in 4-APD electrolyte and the NaF-rich SEI to repress the Na dendrite growth. Reproduced with permission from Ref. [58], © Wiley-VCH GmbH 2022. Analysis of the numbers of different ions in the innermost interfacial layer, (b) Ratio of $[C3mpyr]^+$ to $[FSI]^-$ number and (c) number of Na^+. Reproduced with permission from Ref. [59], © Rakov, D. A. et al. 2020. Illustration of the charge/discharge processes in (d) surface binding energy vs. binding site for NaF (left) and NaBr (right) obtained from JDFT analysis of adatom diffusion. The entire contour plot is generated by symmetry using the data points indicated by cross symbols. Reproduced with permission from Ref. [60], © Choudhury, S. et al. 2017. (e) *In situ* optical observation of Na^+ deposition on Na_3P@Na and bare Na anodes in homemade transparent quartz symmetrical cells at 1.0 mA·cm^{-2}. The scale bar is 100 μm. Reproduced with permission from Ref. [62], © Wiley-VCH GmbH 2020. (f) Schematic illustration of Na plating on NaBrP modified Na and bare Na. Reproduced with permission from Ref. [63], © Elsevier Ltd. 2022. (g) Proposed mechanisms of $NaBH_4$/glyme electrolytes. Reproduced with permission from Ref. [64], © The Royal Society of Chemistry 2022.

combining them can produce the ideal SEI. Ji's group found that Na_3P has semiconductor properties with a band gap of 0.22 eV, resulting in the deposition of Na onto the surface of SEI and the generation of Na dendrites. NaBr has good electronic insulation with a band gap of 3.61 eV, and Na^+ prefers to diffuse along the NaBr interface [63]. Dendrite-free Na metal anode was achieved by combining NaBr with Na_3P in the interface (Fig. 2(f)). The prepared NaBrP=Na electrode showed long-term stability of over 700 h without short circuit, and achieved excellent magnification and cycle stability with a capacity retention rate of 98% after 500 cycles at 5 C in the assembled full cell with $Na_3V_2(PO_4)_3$ cathodes.

In recent work, Lee et al. demonstrated that NaH could serve as a "good SEI layer" in addition to NaF [64]. They found that the "SEI reconstruction" was caused by $NaBH_4$ treatment (Fig. 2(g)). $NaBH_4$ reacts with the natural oxide layer on the surface of Na metal to form NaH (i.e., $4Na_2O + NaBH_4 = 2NaOH + NaBO_2 + 6Na + H_2$; $2NaOH + NaBH_4 = 2NaH + 2H_2 + NaBO_2$). The generated H_2 gas reacted with the Na metal simultaneously to generate NaH (i.e., $2Na + H_2 = 2NaH$). Young's modulus of NaH (~ 45 GPa) is much higher than the required value (5.2 GPa) to prevent the growth of Na dendrites. The electronic insulation property can minimize the decomposition of electrolyte. Then, Na||Na symmetric cells using ether-based electrolyte (1 M $NaBH_4$ in diethylene glycol dimethyl ether (DEGDME)) achieved excellent long-term cycling stability (over 1200 h) at the current density of 1 mA·cm^{-2} with the capacity limitation of 1 mAh·cm^{-2}, which was batter compared to the symmetric cells using F-based electrolyte (1 M $NaClO_4$ in EC/PC + 5 wt.% FEC, or 1 M NaOTf in tetraethylene glycol dimethyl ether (TEGDME)).

The inorganic-rich SEI reduces the diffusion energy barrier of Na ions/atoms, which contributes to uniform distribution of Na^+ flux and homogeneous Na metal deposition. At the same time, the high mechanical strength of inorganic-rich SEI layer prevents the continuous growth of dendrites. In addition to inorganic Na salts, metal oxides (Al_2O_3 and SiO_2) also contribute to the realization of dendrite-free Na metal anodes [65, 66]. Although inorganic-rich SEI layers with sufficient hardness and stiffness can effectively prevent dendrite formation, they may still crack due to the stress caused by the volume change of the Na metal anode, thus requiring a more complex structural design.

2.2 Organic interphase engineering

In general, the organic components of SEI are generated electrochemically from the decomposition of organic solvents in the electrolytes. For example, SEI contains organic components such as RONa, $ROCO_2Na$, and RCOONa in carbonate-based electrolytes [67]. The mechanical stress caused by dendrite growth and volume change can be suppressed by constructing flexible organic protective layer on Na metal surfaces. The functional groups of organic can also increase the adhesion of protective layer and guide uniform Na deposition.

The reactive monomers can be electrochemically polymerized on the metal surface to form functional polymer thin films [68]. Archer et al. first applied this method to Na metal anode

protection by adding IL to the liquid electrolyte [69]. Functional IL monomers were electropolymerized on Na metal to form SEI films (Fig. 3(a)). During charging, the unsaturated IL monomers received electrons to form active species. These species then reacted with the monomers to polymerize and eventually formed a porous film in conformal contact with the Na metal electrode. The film with excellent ionic conductivity could inhibit the parasitic reactions of Na metal anodes with the liquid carbonate electrolytes. The structure, morphology, and polymerization process of the polymer film was affected by the molecular structure of the IL monomer. They investigated imidazole cationic IL monomers with different functions, such as 1-allyl-3-methylimidazolium perchlorate (AMIM), 1,3-diallyl-imidazolium perchlorate (DAIM)), and 1-allyl-3-vinyl imidazolium perchlorate (AVIM). The results showed that AMIM could only form oligomers without forming films due to the limited unsaturated components. The presence of vinyl makes AVIM more reactive and self-aggregative, resulting in a membrane that is less morphic and stable than that formed by DAIM. Adding 20 wt.% DAIM to the electrolyte increased the CE value of Na/stainless steel batteries from 16.7% to 95.0%.

Polyvinylidene fluoride (PVDF) is a commonly used organic material in energy storage field [70, 71]. A simple spatula coating technique was used to construct PVDF coating on the surface of Cu foil [72]. The defluorination reaction between PVDF and Na metal resulted in the formation of NaF and Na_2O_2 rich SEI. As a result, the PVDF@Cu current collector exhibited excellent electrochemical performance: an extremely long life of ~ 1200 h with a small overpotential (~ 35 mV) and a high mean CE of 99.91% for 2000 h at 1 mA·cm^{-2}.

Organosulfur compounds also have great potential in Na metal protection. Wu's groups reported a protective layer rich in Na benzenedithiolate (PhS_2Na_2) [73]. Catalyzed by Na metal, the S_8 in anhydrous tetrahydrofuran reacted with para-dichlorobenzene (p-DB) on the surface of Na metal to form poly(phenylene sulfides) (PPS). PPS was converted to PhS_2Na_2 during the initial cycle of the symmetric cell (Fig. 3(b)). Scanning electron microscopy (SEM) images showed that the surface of the Na metal was uniformly covered by a thin film with the thickness of approximately 5 μm (Fig. 3(c)). Due to the rapid reaction, the protective layer was closely confined with the Na metal, without any voids between

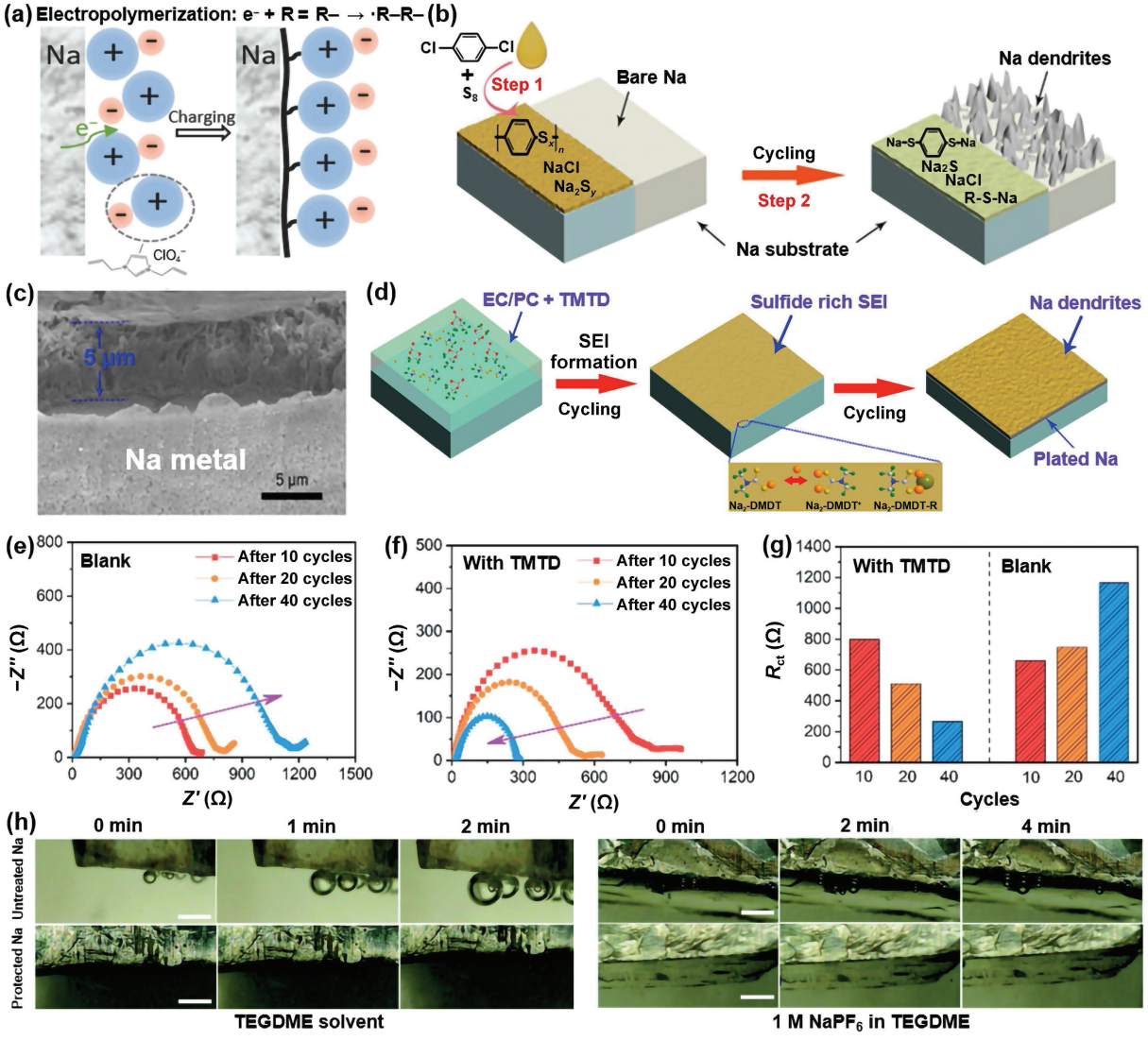

Figure 3 (a) A schematic drawing of the polymeric ionic liquid film formation on the electrode. Reproduced with permission from Ref. [69], © WILEY-VCH Verlag GmbH & Co. KGaA, Weinheim 2017. (b) Diagram for the fabrication of a PhS_2Na_2-rich protection layer on sodium metal foil. (c) SEM image of the protected sodium foil. Reproduced with permission from Ref. [73], © Wiley-VCH Verlag GmbH & Co. KGaA, Weinheim 2020. (d) Schematic illustrations of the evaluation of the sodium metal anode surface morphology in the conventional carbonate electrolyte and TMTD-added electrolyte. The Nyquist plots of the symmetric cells using (e) the TMTD-added electrolyte and (f) the blank electrolyte after cycling. (g) The evaluation of the corresponding R_{ct} values. Reproduced with permission from Ref. [74], © American Chemical Society, 2021. (h) *In situ* digital micrograph images of the cross-sectional surface of untreated Na and protected Na in TEGDME solvent and the electrolyte (1 M $NaPF_6$ in TEGDME), recorded at different times. The scale bar is 0.5 mm, applicable to all images. Reproduced with permission from Ref. [75], © Lu, Q. Q. et al. 2021.

them. The Na||Na symmetric battery with PhS_2Na_2 protection continuously stripped/plated for over 800 h. The full battery cycling performance using Prussian blue as the cathode and PhS_2Na_2 protective Na as the anode was also excellent, providing a stable discharge capacity of 89.5 mAh·g^{-1}, with more than 1000 cycles and a capacity retention rate of 93%. Wu et al. also found that tetramethylthiuram disulfide (TMTD) as an additive could decompose and form a protective layer rich in organic Na sulfide (sodium dimethyldithiocarbamates (Na-DMDT) or Na_2-DMDT-R; R represent an alkyl group) (Fig. 3(d)) [74]. The symmetric cell with 2 wt.% TMTD in the electrolyte cycled for over 1600 h without any signs of short circuit, nearly three times longer than the symmetric cell with blank electrolyte (570 h). Nyquist plots of the symmetrical cell with the electrolyte containing 2 wt.% TMTD and the blank electrolyte were compared in Figs. 3(e)–3(g). The interfacial transport resistance (R_{ct}) of the cell with blank electrolyte increased with the cycle number, reaching nearly 1167 Ω after 40 cycles. The interfacial transport resistance of the cell with TMTD electrolyte was ~ 800 Ω after 10 cycles, but decreased to 511 Ω after 20 cycles and further decreased to approximately 269 Ω after 40 cycles. This was caused by the formation of a stable protective layer via the decomposition of TMTD. The low interfacial transport resistance also indicated that the protective layer promoted Na^+ transport through the layer.

When designing the protective layer, the cost and processing technology are also important factors that need to be considered, which determines whether Na metal anodes can be practically applied to high energy density Na-based batteries. Mikhailova et al. developed a stable protective layer on Na metal by a simple 1,3-dioxolane (DOL) pretreatment method [75]. Energy dispersive X-ray spectroscopy (EDS), X-ray photoelectron spectroscopy (XPS), and Fourier transform infrared (FTIR) spectroscopy analysis showed that the elastic and robust protective layer was mainly composed of poly(DOL)-type materials. The polar oxygen-containing groups in the protective poly(DOL) layer could promote uniform Na^+ deposition. Therefore, the protected Na metal anode showed excellent cycling stability for 2800 h or 1400 cycles, while the overpotential of untreated Na metal anode increased from 25 to 330 mV in the first 200 h. Furthermore, the protective poly(DOL) layer insulates the Na metal from continuous reaction with the electrolyte. The untreated and protected Na metal was immersed in TEGDME. Due to the reactivity of Na, the untreated Na immediately generated gas. However, the gas generated from the reaction between the protected Na and TEGDME was significantly reduced (Fig. 3(h)). In the electrolyte of 1 M $NaPF_6$ in TEGDME, no visible gas bubbles were observed near the surface of the protected Na compared to the untreated Na, further confirming the stability of the protective layer.

Flexible organic protective films have been widely used in Li metal anode protection [76–78], but there are few reports about their application in Na metal batteries. The effects of organic materials in Na metal protection still need to be developed. Because of the highly corrosive nature, Na metal will react irreversibly with the organic protective layer, resulting in a loss of capacity. In addition, the low Young's modulus (low stiffness) makes Na below the organic layer prone to dendrite growth.

2.3 Inorganic–organic composite interphase engineering

Combining the rigidity of organic materials with the flexibility of inorganic materials, the organic–inorganic composite protective layers may not only effectively alleviate the volume expansion through the organic layer, but also improve the uniform diffusion of Na^+ through the inorganic layer [79, 80]. Therefore, organic–inorganic composite protective layers are ideal coatings to regulate Na deposition behavior.

Molecular layer deposition (MLD) technology, similar to ALD technology, can be employed to prepare inorganic–organic hybrid or pure polymer thin films with many advantages, such as adjustable thermal stability and improved mechanical properties [81, 82]. Sun's group used the MLD method to deposit alucone for the first time as a protective layer for Na metal anode [83]. The adsorption energy between alucone and Na metal was very strong (5.50 eV) due to the presence of O–Na and Al–Na bonds. The alucone coating not only helped Na metal anodes form stable SEI layers as the passivating agents, but also allowed repeated Na plating/stripping on Na metal surface with significant roughness due to mechanical flexibility. Therefore, compared with the pristine Na metal anode and Al_2O_3-coated Na metal anode, alucone-coated Na metal anode showed improved electrochemical performance at various current densities. Moreover, alucone film may stabilize the active Na metal anode/electrolyte interface in all-solid-state sodium metal batteries, thereby alleviating the decomposition of sulfide-based electrolytes (Na_3SbS_4 and Na_3PS_4) and inhibiting Na dendrite growth [84]. Although the polymeric alucone layer has been used in Na metal batteries, the alucone layer is unable to promote the long-term cycle of Na-O_2 batteries due to the attack of superoxide species. Sun et al. combined a polymeric alucone film with a chemically stable solid electrolyte (SSE) to achieve a long-life Na-O_2 battery [85]. SSE restores the dendrite suppression function of alucone on the Na metal anode by shielding superoxide from the oxygen cathode. The changes in alucone film were analyzed by time-of-flight secondary ion mass spectrometry (ToF-SIMS) (Fig. 4(a)). Since there are no shuttled superoxide species, the Na@alucone anode after cycling still showed a strong signal of secondary ions (C_2Al^-, $COAl^-$, and C_2OAl^-) from alucone on the outermost surface (Fig. 4(b)), indicating that no decomposition of the alucone film had occurred. In addition, the thickness of the sodiumized alucone layer is approximately 25 nm, an increase from the original thickness (20 nm) (considering the sputtering rate of 0.1 nm·s^{-1}). This observation showed that a new stable SEI layer formed on the surface of the Na@alucone electrode after cycling. A high-performance rechargeable hybrid solid state (HSS) Na-O_2 battery consisting of Na@alucone anode, SSE, and high-efficient cathode provided a long cycle life of 325 cycles at 0.2 mA·cm^{-2} with a limited capacity of 0.2 mAh·cm^{-2}.

Introducing suitable inorganic Na salts to PVDF matrix can improve its mechanical modulus and ionic conductivity, so as to satisfy the requirements of the ideal SEI [86–88]. Jiao et al. prepared a freestanding and implantable artificial protective layer (FIAPL) by mixing NaF granules with PVDF powders (NaF/PVDF mass ratio 4:1) [89]. NaF increased the mechanical strength of the protective layer and homogenized the Na^+ flux. PVDF provided good flexibility and tightened cross-linking with NaF particles (Fig. 4(c)). The Na||Na symmetric cells with the implantable protective layer showed an improved cycling performance of more than 1200 h at a current density of 0.25 mA·cm^{-2}. Metal nanoparticles with high Na affinity have the function of reducing the nucleation overpotential of Na, which is conducive to stabilizing the Na plating/stripping process [90, 91]. Huang et al. prepared a low-cost hybrid protective layer by incorporating Sn nanoparticles into the polymer PVDF [88]. The Na-Sn alloy with high ionic conductivity (6.12×10^{-13} cm^2·s^{-1}) was formed by alloying reaction between Sn and Na during the initial sodiation process. As a result, the cell with the hybrid protective layer coated Cu current collector exhibited a stable cycle Na plating/stripping of 2500 h at 1 mA·cm^{-2}, with a small

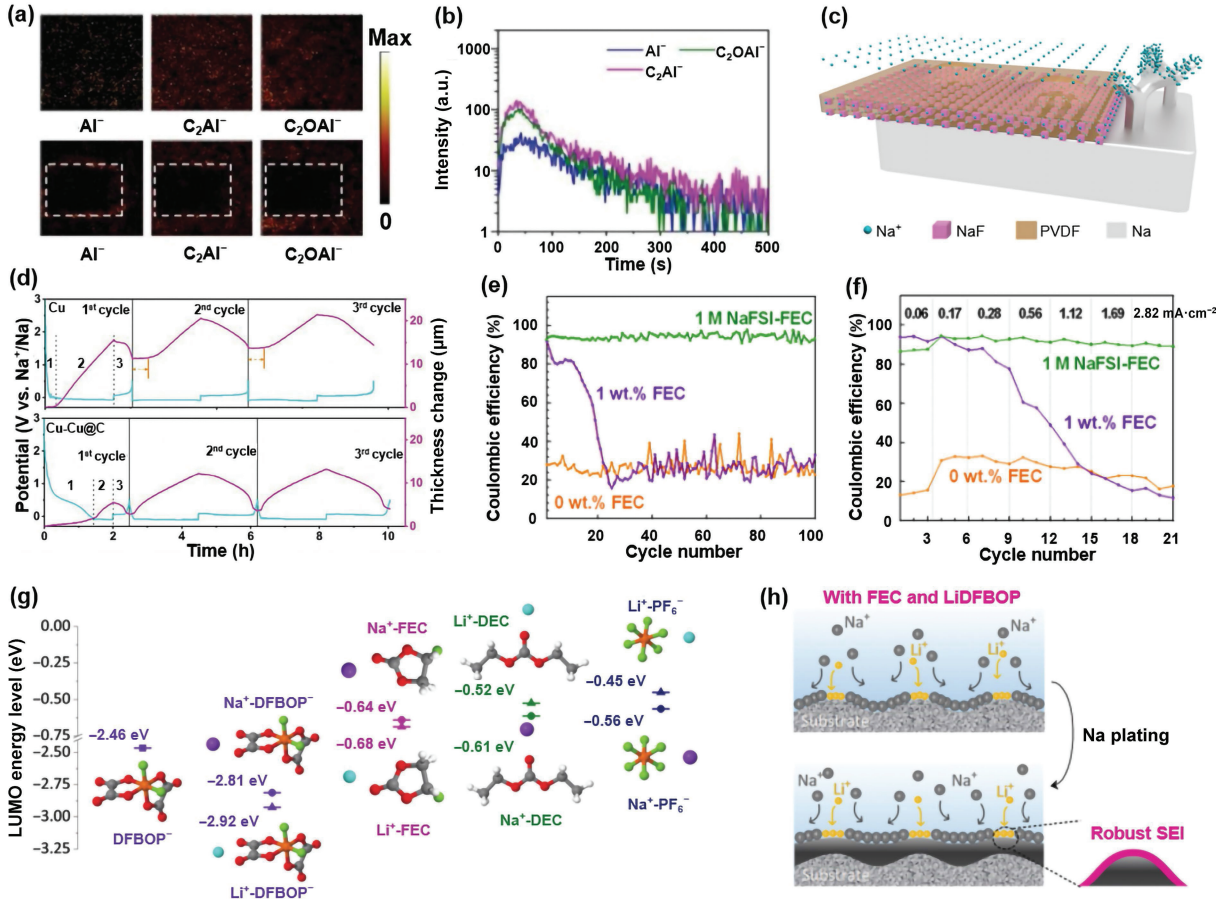

Figure 4 (a) and (b) TOF-SIMS depth profiles and chemical ion images of the Al^-, C_2Al^-, and C_2OAl^- species for the cycled Na@alucone anode obtained from Na-O_2 cell with SSE. Reproduced with permission from Fef. [85], © Wiley-VCH GmbH 2021. (c) Schematic diagram of the FIAPL mechanism. Reproduced with permission from Ref. [89], © American Chemical Society 2020. (d) *In situ* dilatometry investigation of bare Cu and Cu-Cu@C at a current density of 0.5 mA·cm^{-2} and with a Na plating charge fixed at 1 mAh·cm^{-2}: voltage profile and corresponding thickness change of bare Cu and Cu-Cu@C during the first three cycles. Reproduced with permission from Ref. [94], © Li, H. H. et al. 2022. (e) CE of Na/Cu coin-type cells in 1 M NaFSI-EC/PC (1/1), 1 M NaFSI-EC/PC (1/1) + 1 wt.% FEC, and 1 M NaFSI-FEC at 0.28 mA·cm^{-2}. (f) Rate capability of Na/Cu coin-type cells evaluated at the same current density for the Na plating and stripping process. Reproduced with permission from Ref. [97], © American Chemical Society 2018. (g) LUMO energy levels of $DFBOP^-$, Na^+-$DFBOP^-$, Li^+-$DFBOP^-$, Na^+-FEC, Li^+-FEC, Na^+-DEC, Li^+-DEC, Na^+-PF_6^-, and Li^+-PF_6^- complexes obtained by DFT calculations. (h) Schematic illustration of the Na plating process in the electrolyte with FEC and LiDFBOP. The enlarged image on the right side shows the interfacial state of electro-deposited Na. Reproduced with permission from Ref. [104], © The Royal Society of Chemistry 2022.

overpotential (~ 40 mV). Moreover, a high CE of 99.73% was achieved for 2800 h at 2 mA·cm^{-2}.

Metal-organic frameworks (MOFs) have the advantages of controllable crystal structure, large surface area, and adjustable pore size, and their application in energy storage materials has aroused extensive research interest [92, 93]. Passerini et al. investigated the effect of Cu-based MOF (Cu-BTC)-derived composite (Cu@C) on Na plating/stripping behavior employing *in situ* electrochemical dilatometry [94]. The changes in electrode thickness (magenta lines) for the bare copper and Cu-Cu@C electrodes during the first three cycles are shown in Fig. 4(d). The voltage curves are also shown in cyan lines. As seen, the thickness of Cu-Cu@C electrode increased and shrank very closely, and the reversibility was higher than 99.9%. However, due to the accumulation of "dead Na", the bare Cu showed irreversible thickness expansion with an average rate of ~ 1 μm per cycle. The result showed that Cu@C layer was conducive to the formation of dense Na depositions and inhibited the thickness increase due to the accumulation of "dead Na", resulting in the good cyclic stability during Na plating/stripping.

Numerous studies have shown that FEC contributes to the formation of a stable protective layer on the surface of metal electrodes [95, 96]. Choi and coworkers reported an electrolyte containing the FEC solvent and the Na fluoride (NaFSI) salt [97]. The FEC-derived ionic interlayer, including R-OCO_2Na, anhydride (CO_2-CO) containing compounds, Na_2CO_3, and NaF, were identified by *ex situ* XPS. FEC significantly improved the CE (94%) and the cycling performance of Na|Cu half cells (Fig. 4(e)). However, FEC as an additive could not cover the Na metal surface completely because of consumption upon cycling, resulting in a rapid decline in cycling performance. However, using FEC as the main solvent could form a long-term stable interface layer on Na metal, and could even repair the damaged interface layer. The increase in FEC content could also improve the cycling performance of Na|Cu batteries at high current density (Fig. 4(f)).

In ultra-low concentration electrolytes (ULCE), more EC solvents preferentially decompose to form a more flexible interfacial layer. However, due to the low shear modulus, the SEI layer dominated by organic species cannot effectively inhibit the growth of Na dendrites [98]. After adding N,O-bis(trimethylsilyl) trifluoroacetamide (BSTFA) into ULCE, a stable SEI layer containing mainly organic species and rich NaF was formed on the surface of Na metal anode by C=N polymerization during cycling, which could promote the reaction kinetics and improve interface stability [99]. Therefore, Na||$Na_3V_2(PO_4)_3$ (NVP) cells showed a long cycle life and high-rate performance, with a capacity retention of 92.63% after 1955 cycles at 2 C, and a superior rate capability of exceeding a discharge capacity of

105 mAh·g^{-1} at 40 C. This method is convenient by adding additives to promote the formation of organic/inorganic hybrid layers on the metal surface [100]. Besides, Archer et al. found that SiO_2-IL-ClO_4 particles as an electrolyte additive could improve the stability of Na-S batteries [101]. Electron microscopy and electrochemical analysis indicate that the particles constituted a dense and mechanically strong SEI layer on Na metal anode, protecting the Na metal from the corrosive liquid carbonate electrolyte. In addition, SiO_2 particles, as the anchor points for ClO_4^- anion, could facilitate the Na deposition process by tethering anion effect. Thus, the CE of the cell with only small amounts of SiO_2-IL-ClO_4 as the electrolyte additive could be increased to over 90% in each cycle, and the CE could be further enhanced with the increase of SiO_2-IL-ClO_4 content in the electrolyte.

Homogenizing the electric field distribution at the surface of Na metal anodes by electrostatic shielding is one of the effective strategies to suppress Na dendrite formation [102, 103]. Xia's group used a multifunctional additive, lithium difluorobis (oxalato) phosphate (LiDFBOP) to improve the electrochemical performance of Na metal anodes [104]. The Li^+ improved electrolyte stability by forming solvated structures with other molecules (such as $DFBOP^-$ and FEC) in the electrolyte. There are differences in the overall lowest unoccupied molecular orbital (LUMO) energy levels of molecules and complexes coordinated by different cations. Since Li^+ has one less electron shell than Na^+, the binding energy of Li^+ to solvent molecules is much stronger. When molecules solvated Li^+, the corresponding LUMO and FEC energy levels were lower (Fig. 4(g)). Thus $DFBOP^-$ and FEC preferentially acquired electrons to form SEI and inhibit the decomposition of diethyl carbonate (DEC) and PF_6^-. Moreover, due to strong electrostatic attraction, Li^+ preferentially adsorbed on the projection of the matrix or the dendrite tip, and then deposited Na^+ into the area near the dendrite tip through electrostatic repulsion, thus inhibiting the formation of Na dendrite. $DFBOP^-$ reduction formed stable and robust organic/inorganic hybrid interphase, which further inhibited Na dendrite growth and can inhibit subsequent electrolyte decomposition (Fig. 4(h)). The Na||$Na_3V_2(PO_4)_2F_3$ full cell with LiDFBOP could operate well at high voltages up to 4.5 V. Such a full cell presented a high energy density of 295 Wh·kg^{-1} at 1 C (based on total cathode/anode masses) and had impressive cycle performance (maintaining 90% of its initial capacity after 220 cycles with a high average CE of 99.5%), excellent rate ability (10 C), and a reasonable operating temperature range (−20 to 60 °C).

In conclusion, cycling stability of Na metal anodes can be improved significantly through rational interface engineering. In order to clarify the protection effect, the electrochemical performance of interface engineering was summarized and compared from the aspects of material, technique, electrolyte, current density, electroplating/stripping capacity, CE, and cycle life (Table 1). Considering the practical application of Na metal anodes, the ideal protective layer should have the following advantages: (1) high Na^+ conductivity; (2) low electron conductivity; (3) sufficient mechanical strength; (4) uniform and sufficient sodiophilic sites; and (5) low cost and industrial scalability. However, there is currently no unified standard for material selection, thickness, and density of interface layers. In addition, most of the studies on interface engineering are based on excess Na, and relatively few reports on the construction of protective layers on ultra-thin Na films. This means that researchers still need to explore further, from materials to preparation processes. More importantly, the structure–function relationship between SEI and Na metal anodes is still not fully understood, which hinders the further development of interface engineering design.

3 Structure designs of 3D current collectors

The scale and distribution of local current density may affect the electrodeposition behavior of Na. Usually, large local currents contribute to tip deposition, which causes dendrite growth. The 3D host with a high surface area can decrease local current density, thus reducing the nucleation barrier and promoting uniform distribution of Na^+ flux. Meanwhile, the larger internal space of 3D current collectors also mitigates the volume change of the anode during cycling, thereby alleviating the crack of the SEI [19, 33]. With these advantages, the 3D host design also shows great research value and application prospect in improving Na nucleation and electroplating behavior. In this section, the recent development of high-conductivity 3D metal-based frameworks, lightweight 3D carbon-based frameworks, and "gradient sodiophilic" 3D composite frameworks have been summarized.

3.1 3D metal-based current collectors

On the traditional planar metal (Cu and Al) current collector, the distribution of electrons is consistent with the geometric shape of the current collector surface. Due to the inevitable activity difference of planar sites, it is difficult for electrons to distribute uniformly [105]. The inhomogeneous electric field causes the uneven deposition of Na^+, resulting in local aggregation of Na to form dendrites. An effective strategy to solve these problems is to use 3D instead of planar current collectors, thereby improving the local distribution of the electric field [106]. Copper foam in commercial current collectors can be used as an excellent substrate for Na deposition because of its excellent mechanical properties and rich three-dimensional porous structure [107]. However, due to its "sodiophobic" nature, there is only weak physical absorption between Na and copper foam. The surface of copper foam is treated by oxidation or vulcanization to promote the impregnation and uniform distribution of molten Na throughout the matrix, thus forming more stable anode hosts. Porous Al foil can serve as the substrate for Na dendrite inhibition and is superior to copper foil in terms of cost and weight [108]. Na metal anodes can operate stably on porous Al foil for over 1000 cycles, with an average Coulomb efficiency higher than 99.9%. In addition to Cu and Al, porous 3D Ni is also an effective scheme to inhibit the formation of harmful dendrites [32].

Due to the high deposition barrier and surface diffusion barrier, these conventional 3D hosts do not achieve essentially uniform Na nucleation. One of the most direct ways to solve this problem is to design 3D porous frames with "sodiophilic" surfaces [109, 110]. Peng et al. reported a 3D Cu foam skeleton with hierarchical ZnO nanorod arrays (CF@ZnO) as a stable host for Na metal anodes (Fig. 5(a)) [111]. Compared with traditional 3D Cu foams, the highly sodiophilic ZnO nanorods on CF@ZnO provided abundant Na nucleation sites and significantly reduced Na nucleation overpotential. Therefore, Na was preferentially deposited on the surface of ZnO nanorods. Due to the increase in deposition area, the current density in the channel and substrate decreases, resulting in uniform Na^+ flux on the electrolyte/electrode contact surface. Yu's group proposed a 3D porous Cu skeleton modified by Cu_2Se nanosheets (Fig. 5(b)) [112]. CF/Cu_2Se was immersed in molten Na, and Cu_2Se nanosheets promoted Na penetration through siphon effect. More importantly, the fused Na will undergo a conversion reaction with Cu_2Se to produce Na_2Se and Cu ($2Na + Cu_2Se = 2Cu + Na_2Se$). The Gibbs free energy change (ΔG) of the reaction was calculated by thermochemical analysis as −60.1 kcal·mol^{-1}, indicating that the

Table 1 Summary of the reported literature on interface engineering of sodium metal anodes[a]

Na cells	Material	Technique	Electrolyte	Current density ($mA·cm^{-2}$)	Capacity ($mAh·cm^{-2}$)	CE (%)	Lifespan	References
Na-Na	NaF	Reacting with PTFE	1 M $NaCF_3SO_3$ DEGDME	5	1	—	600 h	[49]
Na-Cu	NaF Na_2O	$NaPF_6$	1 M $NaPF_6$ diglyme	0.5	1	99.9	300 cycles	[51]
Na-Cu	NaF	Highly-fluorinated structure	1.0 M $NaPF_6$ FEC/PC/HFE + 5 vol.% PFMP	0.5	1	~ 99.4	1100 h	[54]
Na-Cu	NaF	Adding 4-APD	1 M $NaPF_6$ EC/DEC + 1 wt.% 4-APD	1	1	86.3	500 h	[58]
Na-Na	NaF	High salt concentration, preconditioning potential	50 mol% NaFSI C3mpyrFSI	5	0.1	—	700 cycles	[59]
Na-Na Na-Cu	NaBr	Reacting with bromopropane	1 M $NaPF_6$ EC/PC	0.25/0.5/1	0.25/0.5/1	> 99	250 h 250 cycles	[60]
Na-Na Na-Cu	NaI	Iodine-containing *in situ* reaction	1 M $NaClO_4$ EC/DEC + 5% FEC	0.25	0.75	99.33	500 h 350 cycles	[61]
Na-Na	Na_3P	Reacting with red P	1.0 M NaTFSI FEC/EMC	1	1	—	780 h	[62]
Na-Na	NaBrP	Reacting with PBr_3	1 M $NaPF_6$ EC/DEC + 5% FEC	1	1	—	700 h	[63]
Na-Na Na-Al	NaH	Reacting with $NaBO_2$	1 M $NaBH_4$ DEGDME	1	1	99.67	1200 h	[64]
Na-Na	Al_2O_3	PEALD	1.0 M $NaClO_4$ EC/DEC	0.25	1	—	450 h	[65]
Na-steel	Polymer film	Adding AVIM	1 M $NaClO_4$ EC/PC + 20 wt.% DAIM	0.1	—	95.0	~ 2200 h	[69]
Na-Cu	PVDF	Coating	1 M $NaPF_6$ DGM	1	1	99.91	2000 h	[72]
Na-Na	PhS_2Na_2	Adding DPDS	1 M $NaPF_6$ EC/PC + 1 wt.% DPDS	1	1	—	800 h	[73]
Na-Na	Na-DMDT	Adding TMTD	1 M $NaPF_6$ EC/PC + 2 wt.% TMTD	0.25	0.25	94.25	1600 h	[74]
Na-Na	DOL	Reacting with DOL (BASF)	1 M $NaPF_6$ TEGDME	1	1	—	2800 h	[75]
Na-Cu	NaF, Na_2O, and O–B–O	$NaBF_4$	0.64 M $NaBF_4$ diglyme	0.5	1	99.93	400 cycles	[80]
Na-Na	Alucone	MLD	1 M $NaPF_6$ EC/PC	1	1	—	270 h	[83]
Na-Na	Alucone	MLD	c-Na_3PS_4	0.1	0.1	—	475 h	[84]
Na-O_2	Alucone	MLD	$Na_{3.25}Zr2Si_{2.25}P_{0.75}O_{12}$ SSE	0.2	0.2	—	325 cycles	[85]
Na-Na	Al_2O_3-PVdF-HFP	Roll pressing	1 M $NaClO_4$ EC/PC	0.5	1	—	~ 550 h	[87]
Na-Cu	Sn-PVDF	Doctor blade coating	1 M $NaPF_6$ DGM	2	1	99.73	2800 h	[88]
Na-Al	NaF-PVDF	FIAPL	1 M NaTFSI FEC	0.25	0.5	96	100 cycles	[89]
Na-Cu	PVDF-Bi	Doctor blade coating	1 M $NaPF_6$ diglyme	1	2	99.92	2500 cycles	[90]
Na-Cu	MOF-199	Coating	1 M $NaClO_4$ EC/DMC + 5% FEC	1	1	80	25 cycles	[93]
Na-Cu	NaF, R-OCO_2Na, CO_2-CO-, and Na_2CO_3	FEC	1 M NaFSI FEC	0.28	2.82	94	100 cycles	[97]
Na-Na	C=N, NaF	Adding BSTFA	0.3 M $NaPF_6$ EC/PC + 2 wt.% BSTFA	0.5	—	—	300 h	[99]
Na-Al Na-Na	NaF, Na_2S, Na_2SO_3, organic S-containing salts, and Na_3PO_4	Adding DTD	TMP/FEC/ DTD-E	0.5 1	0.5 0.5	94.56	250 cycles 1350 h	[100]
Na-Ag Na-Na	$C_2O_4^{2-}$, Na-O, CO_3^{2-}, NaF, and PO_yFz_x	Adding LiDFBOP	1 M $NaPF_6$ FEC/DEC + 0.5 wt.% LiDFBOP	0.5 1	0.5 1	98.6	300 cycles 2600 h	[104]

[a]PTFE = poly(tetrafluoroethylene); EMC = ethyl methyl carbonate; PEALD = plasma-enhanced ALD; DGM = diethylene glycol dimethyl ether; DPDS = diphenyl disulfide; DMC = dimethyl carbonate; DTD = 1,3,2-dioxathiolane 2,2-dioxide; and TMP = trimethyl phosphate.

reaction was spontaneous. Na_2Se/Cu nanosheets could promote Na^+ migration and induce Na nucleation. Metal selenides with high conductivity are beneficial for redistributing ionic concentration due to faster electrode reaction kinetics. The Na_2Se/Cu@Na composite anode symmetric cell presented a polarization voltage value of ~ 70 mV and a long cycle life of over 500 h at a current density of 1 $mA·cm^{-2}$ and a fixed capacity of 1 $mAh·cm^{-2}$.

The high binding energy between the alloy and Na^+ can induce abundant and uniform active sites to achieve a uniform and dense deposition of Na layer. However, the high electronic conductivity of the alloy can cause the deposition of Na on the top surface of the framework. The construction of an electron passivated and ion conduction surface layer on the top of the scaffold made Na^+ diffuse and deposit in the skeleton, preventing the growth of dendrites. Peng et al. introduced a SnO_2-coated porous sodiophilic zinc metal framework on a copper substrate (Cu/Zn/SnO_2) [113]. Before Na^+ deposition, Zn reacted with Na to transform into Na-Zn alloy. After the first cycle, the top SnO_2 and Na were electrochemically reacted to form Na-Sn alloy and Na_2O. The electrically insulated Na_2O not only prevented the deposition of Na^+ on the top of framework, but also facilitated the formation of

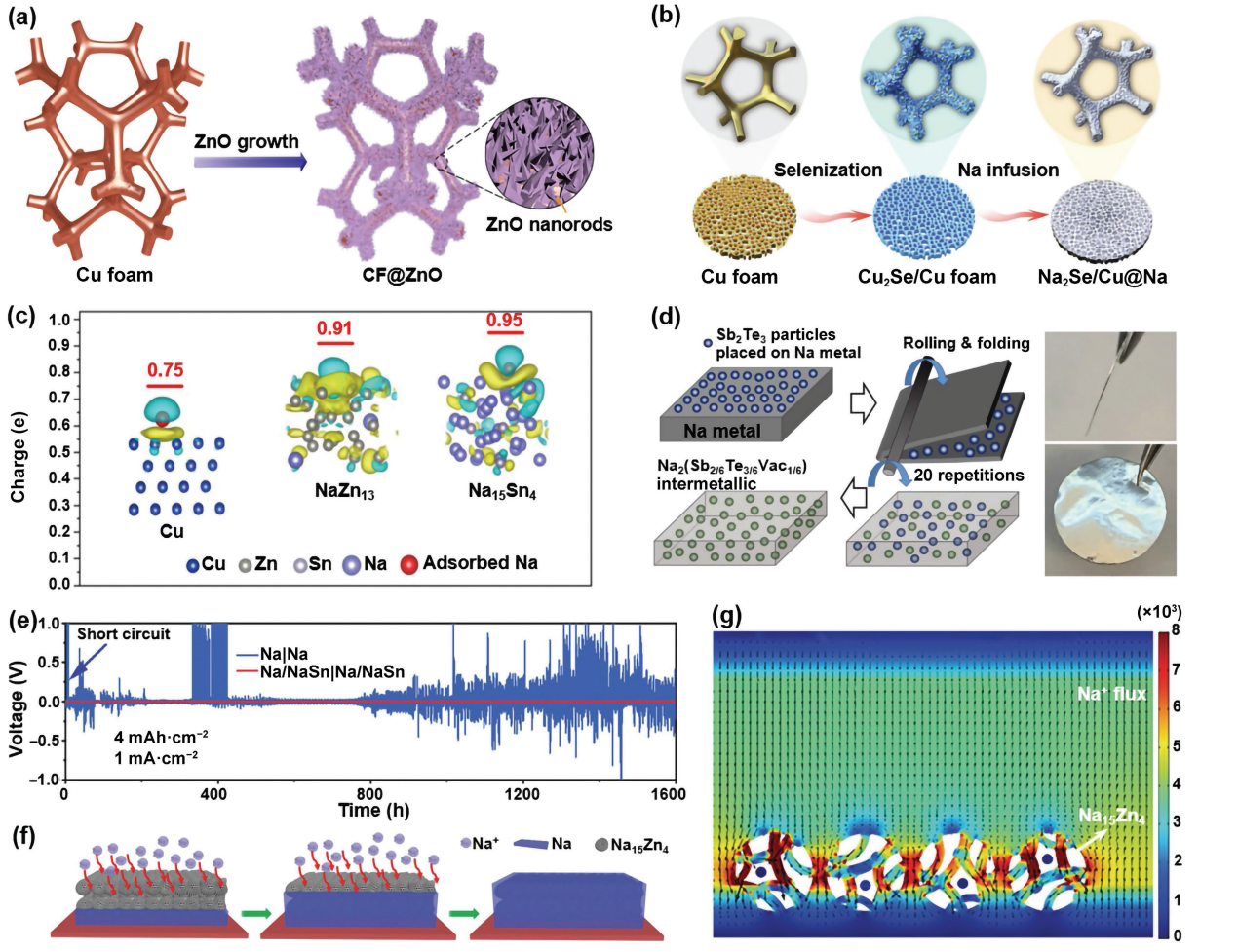

Figure 5 (a) Schematic of the preparation process for CF@ZnO. Reproduced with permission from Ref. [111], © Elsevier Ltd. 2020. (b) The illustration of the synthesis process of Na_2Se/Cu@Na composite anode. Reproduced with permission from Ref. [112], © Wiley-VCH GmbH 2022. (c) The turquoise and yellow regions indicate depletion and accumulation of electrons, respectively. For interpretation of the references to colour in this figure legend, the reader is referred to the web version of this article. Reproduced with permission from Ref. [113], © Elsevier B.V. 2020. (d) (Left) illustration for the fabrication process of NST-Na. (Right) photographs taken inside the glove box of the 150 μm thick self-standing NST-Na foil. Reproduced with permission from Ref. [116], © Wiley-VCH GmbH 2021. (e) The stripping/plating curves for Na||Na and Na/NaSn||Na/NaSn symmetrical batteries. (f) The mechanism of Na deposition on Na/NaSn alloy framework. (g) The section view of numerical simulation of Na^+ flux. Reproduced with permission from Ref. [117], © Jin, Q. Z. et al. 2022.

a stable SEI layer. Na-Zn and Na-Sn were beneficial in reducing the nucleation overpotential of Na deposition. The charge transfer from Na to Cu, $NaZn_{13}$, and $Na_{15}Sn_4$ was calculated by DFT as 0.75, 0.91, and 0.95 eV, respectively (Fig. 5(c)). The larger charge transfer between Na^+ and the alloy scaffold surface results in higher binding energy. The high binding energy of Na and the alloy scaffold helps to reduce the nucleation barrier. The nucleation overpotential of Na^+ deposited on Cu/SnO_2, Cu/Zn, and Cu/Zn/SnO_2 was about 18.1, 15.3, and 8.6 mV, respectively, much lower than that of Cu (52.9 mV).

The method of *in situ* synthesis of 3D alloy networks by mixing sodiophilic metal particles into Na metal is also promising [114, 115]. The Sb_2Te_3 powder and Na metal foil were rolled and folded through 20 iterations to produce a foil with a smooth and bright surface (Fig. 5(d)) [116]. In this process, all Sb_2Te_3 fully reacted with Na and *in situ* formed the Na antimony telluride intermetallic-Na metal composite (NST-Na). NST was a skeleton structure composed of dense and stable Na antimony telluride crystallites ($Na_2(Sb_{2/6}Te_{3/6}Vac_{1/6})$). The filling density and related porosity of the NST skeleton were related to the initial Sb_2Te_3 content. More Sb_2Te_3 increased the weight and volume fraction of the NST skeleton in the composite material, providing more surface area for Na metal plating/stripping. The new intermetallic skeleton had advanced electrochemical properties. NST-Na achieved 100% depth-of-discharge (DOD) and an average CE of 99.4% for 1000 h electroplating/stripping at 1 mA·cm^{-2}. In recent work, Jing et al. reported a metallic Na foil (Na/NaSn) with 3D connection network integrating Na metal and $Na_{15}Sn_4$ alloy through an *in situ* alloy reaction [117]. The alloy $Na_{15}Sn_4$ with high electrochemical potential was less reactive with electrolytes and exhibited an extremely long cycle life due to less electrolyte consumption (Fig. 5(e)). The deposition mechanism of Na metal on the Na-Sn alloy includes: Na^+ is first adsorbed on the surface of $Na_{15}Sn_4$ through solid–liquid interface, and then penetrates the entire Na-Sn alloy network into the Na substrate, and finally forms the Na deposition layer (Fig. 5(f)). The strong affinity between $Na_{15}Sn_4$ alloy and Na^+ makes Na^+ flux tend to accumulate on $Na_{15}Sn_4$ surface. The porous structure with additional electric field can increase the Na^+ flux for planar Na deposition (Fig. 5(g)). The potential difference (~ 0.1 V) between Na and $Na_{15}Sn_4$ could drive the Na^+ transfer through the $Na_{15}Sn_4$ layer. Moreover, the interconnected alloy network may optimize the electric field distribution, and the uniformly deposited Na can still form a plane even when the plating capacity increases.

The conductive metal skeletons have been proven to be excellent hosts for Na deposition. However, the large nucleation barrier prevents the uniform deposition of Na ions/atoms. Generally, surface modification can effectively improve the affinity of metal frames for Na. The overpotential of Na nucleation can also be decreased by alloying. However, it should be noted that

excessive alloy may aggravate the volume change of the anode and lead to the reduction of cycle stability. In addition, the significant weight of metal-based current collectors hinders their application in high energy density batteries.

3.2 3D carbon-based current collectors

Carbon-based materials are commonly used in energy storage systems because of their advantages of light weight and low cost. Carbon has many allotropes with different structures, such as carbon nanotubes (CNTs), carbon fibers (CFs), graphene (Gr), fullerene, and porous carbon [17, 118–122]. The cross-linking 3D network structure of these carbon-based materials has excellent stability and high electronic conductivity. The pores in the structure can also reserve space for Na deposition, effectively buffering the volume change of the anode. In addition, the flexible structure and surface chemistry of the carbon-based framework can regulate the Na deposition behavior and effectively inhibit the growth of Na dendrites.

Defects in the carbon structure can enhance the sodiophilic properties of the carbon skeleton by promoting the interaction with Na^+, which may play a more important role than porosity in inducing uniform metal deposition [123, 124]. Kim et al. employed the DFT calculation to simulate the adsorption and nucleation behavior of Na atoms in the presence of defects on a graphite plane [125]. By placing Na atoms in different positions, the influence of defect on the adsorption behavior of nearby Na atoms was discussed (Fig. 6(a)). The adsorption energy of graphite with defects was much higher than that of the defect-free graphite structure (C_g) at all locations (Fig. 6(b)). Interestingly, when the Na atom was introduced into position 7 (two diagonal unit cell lengths from the defect site), the atom did not migrate to the defect center despite the high adsorption energy (−1.74 eV). This indicated that the defect did not cause the complete aggregation of adsorbed Na atoms at the defect site, avoiding dendrite growth. They designed lignin-derived skeleton carbon nanofibers (SCNFs). The defect-rich and hierarchically porous structure endowed the carbonaceous body super-sodiophilic nature, allowing convenient preparation of SCNF@Na composite anodes. When directly permeated with Na metal at 180 °C, SCNF mat could rapidly absorb Na and become fully saturated in less than 3 s (Fig. 6(c)). In addition, SCNF@Na composite anodes had a high CE (99.3%) and excellent electrochemical reversibility in asymmetric and symmetric cells.

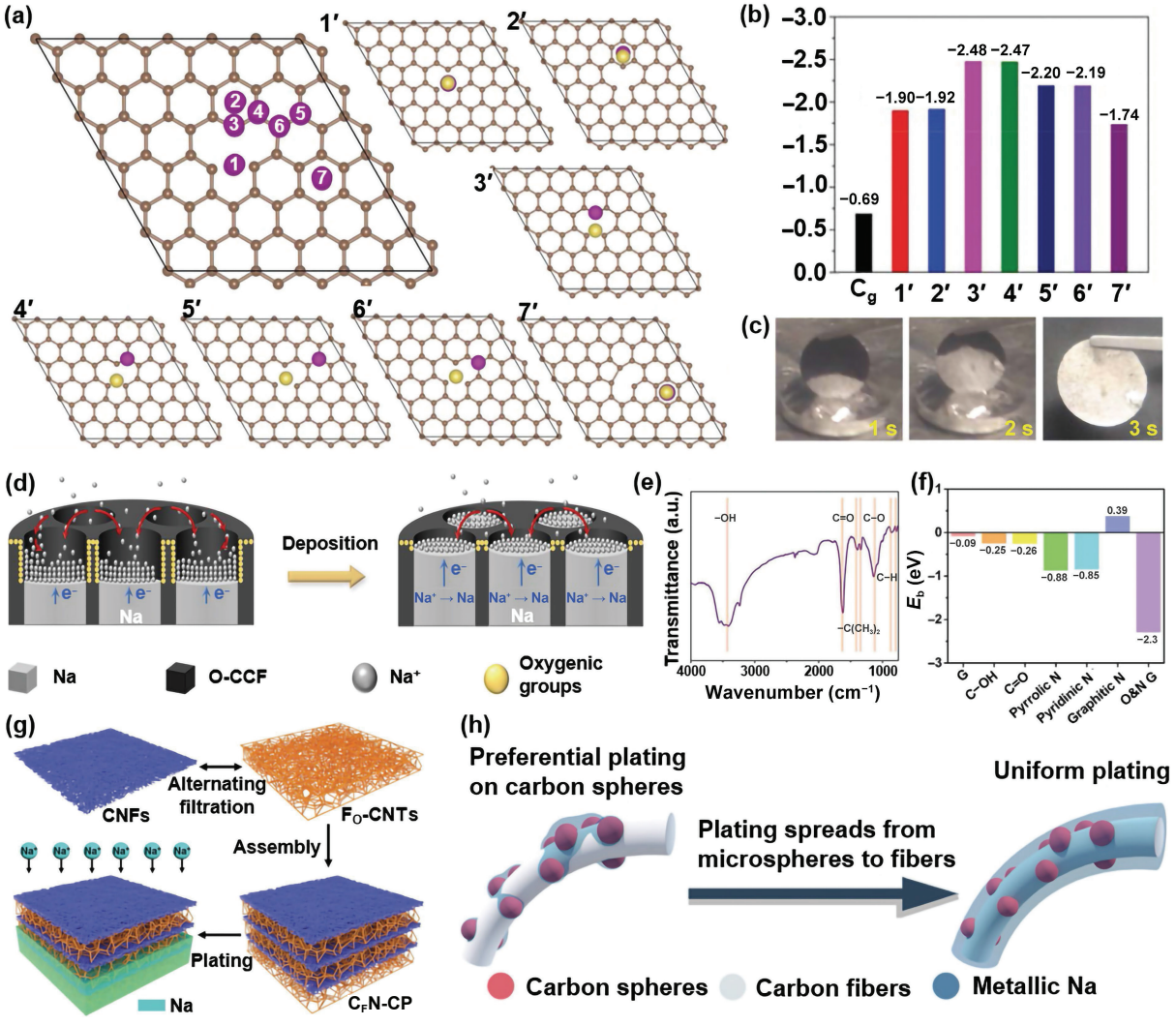

Figure 6 (a) DFT calculations reveal the influence of defects on adsorption behavior of Na atoms in their vicinity. Purple circles with numbers indicate the initial positions at which the Na atoms are placed. Equivalent numbers with a superscript "′" indicate the positions of Na atoms (yellow) in the final relaxed structure. Brown spheres represent carbon structure. (b) Adsorption energies of Na atoms on pristine graphite and defective carbon at different positions. (c) Digital time-lapse images of rapid infiltration of molten Na into SCNF host. Reproduced with permission from Ref. [125], © Wiley-VCH GmbH 2022. (d) Schematic diagram of the structural changes of Na-O-CCF electrodes. (e) FTIR spectra. Reproduced with permission from Ref. [127], © Wiley-VCH GmbH 2020. (f) Binding energies of Na atom with G and different functional groups modified G. Reproduced with permission from Ref. [130], © Wiley-VCH GmbH 2021. (g) Schematic illustration for the preparation of F_O-CNTs and Na@C_FN-CP composite anode. Reproduced with permission from Ref. [133], © Wiley-VCH GmbH 2022. (h) Schematic illustration of the uniform Na plating induced by the proposed 3D "gradient sodiophilic" skeleton. Reproduced with permission from Ref. [135], © Wiley-VCH GmbH 2021.

Carbon materials with sodiophilic functional groups not only have strong interaction with Na^+, but also can regulate the deposition behavior of Na^+ [126]. Xiong et al. for the first time prepared an oxygen-containing carbonized coconut framework (O-CCF) with a unique 3D tubular structure from biomass waste coconut coat, which has a large surface area and can make the electric field evenly distributed (Fig. 6(d)) [127]. The O-CCF contains a large amount of oxygen-containing functional groups (including C–O, C=O, OH, and COOH), which contribute to the improvement of surface sodiophilicity (Fig. 6(e)). Therefore, the nucleation overpotential of O-CCF was only 9 mV, which is much smaller than that of bare copper (74 mV) and CCF (17.3 mV). At the current density of 5 mA·cm^{-2} and an areal capacity of 10 mAh·cm^{-2}, the O-CCF was able to stabilize 1000 cycles with an average CE of 99.6%. Even at the high current density of 50 mA·cm^{-2}, the Na-O-CCF anode showed excellent cyclic stability and low hysteria after 1000 cycles. It is also a common method to synthesize 3D nitrogen (N)-doped carbon bodies using polyacrylonitrile (PAN) as the raw material by electrospinning [128, 129]. Nitrogen containing-functional groups can reduce the nuclear barrier formation and improve the stability of the Na metal anodes in the long cycle process. The sodiophilic properties of carbon scaffolds were increased by multiple functional group modifications [130]. Studies by Jiao et al. showed that graphene modified by O and N together interacts much more strongly with Na^+ than graphene modified by O or N (Fig. 6(f)), which effectively promotes the reaction kinetics.

Elements (e.g., O, N, and S) doped carbon-based subjects have the function of reducing nucleation overpotential and assisting in the generation of more stable SEI [31, 131, 132]. Qiu et al. reported a novel strategy to achieve fluorine-super-doped carbon nanotubes (F_O-CNTs) [133]. Commercial CNTs were first oxidized with concentrated nitric acid and then treated with CF_4 plasma to obtain F_O-CNTs (Fig. 6(g)). The fluoride content of F_O-CNTs (14.38 at.%) was much higher than that of conventional fluorine-doped CNT (5.84 at.%). High fluorine content can promote the formation of an SEI layer dominated by NaF. The new defects caused by O and F engraving ensured the rapid transport of Na^+ and provided more nucleation sites for uniform Na deposition. F_O-CNTs were alternately assembled with cellulose nanofibers (CNF) to produce sandwich-structured composite paper (C_FN-CP). Periodically assembled conductive/dielectric composite papers exhibited excellent flexibility and mechanical properties, leading to strain relaxation-induced uniform Na nucleation and "bottom-up" oriented Na deposition. Based on these advantages, the Na@C_FN-CP electrode had ultra-long cycle stability of over 2100 h with low voltage hysteresis (~ 16 mV) at 1 mA·cm^{-2}.

With the deepening of the cognition of Na deposition and nucleation behavior, it is increasingly popular to design a "gradient sodiophilic" structure to achieve stable Na plating/stripping [91]. The "gradient sodiophilic" skeleton typically consists of conductive matrices and sodiophilic nucleation sites distributed at the bottom or inside of the matrix. During the plating process, Na preferentially deposits at the sodiophilic sites and then spreads to the matrix. The Na metal stripping process is completely opposite to the plating process. The highly reversible gradient plating/stripping process can effectively prevent dendrite formation and improve the CEs of Na metal anodes [134]. In addition, the conductive matrix can improve the homogeneous electric field distribution, which is conducive to the uniform deposition of Na metal in the skeleton. Therefore, the skeleton with "gradient sodiophilic" characteristics can effectively prevent the occurrence of random Na nucleation and the growth of Na dendrites. Xu et al. first proposed to regulate Na deposition behavior by constructing 3D carbon fiber skeletons (CMFS) with abundant defects and "gradient sodiophilic" characteristic [135]. The CMFS consisted of carbon fibers covered by carbon nanospheres. Carbon fibers exhibited parallel long carbon layers, indicating more-developed graphitic structure. Instead, carbon spheres showed randomly oriented short carbon layers, indicating they were more disordered. The ratio between D-band and G-band (I_D/I_G value) in Raman spectra can reflect the defect concentration of carbon materials. The I_D/I_G value of CMFS is 2.09, which was higher than that of carbon fiber skeletons (1.57). The presence of carbon spheres in CMFS substrate increased the defects in the 3D structures. More importantly, the difference in disorder and defect concentration between carbon fiber and carbon spheres contributes to the "gradient sodiophilic" feature of CMFS. As a result, Na preferentially deposited on the more disordered carbon spheres, then diffused to the carbon fibers, and finally gradually expanded to the entire electrode (Fig. 6(h)), without the formation of Na dendrites. The CMFS electrode exhibited an extremely low and stable overpotential (12 mV) and a high average CE (99.96%) for over 1000 h at 5 mA·cm^{-2}.

The lightweight 3D carbon-based current collector demonstrates great application potential in the next-generation high-performance Na metal anodes. According to the above statement, uniform Na nucleation and dendrite growth can be prevented by adjusting the structure, surface chemistry, and spatial distribution of the carbon-based skeleton. Carbon materials have poor wettability to Na metal, resulting in high Na nucleation overpotential [33]. Defects, functional groups, and dopants can provide abundant active sites for uniform Na deposition. However, the affinity of defects for Na is relatively weak. Low amounts of functional groups and heteroatoms also have a limited effect on the enhancement of sodiophilic. Therefore, more novel methods are still needed to improve the sodiophilicity of 3D carbon-based current collectors.

3.3 3D composite current collectors

In recent years, more comprehensive 3D composite current collectors have shown more promising research value. The composite frame has various structures, including metal substrate combined with porous carbon or introducing metal particles into the carbon matrix to form sodiophilic sites [33]. Therefore, the 3D composite framework, which has more sodiophilic metals with the light carbon-based skeletons, can serve as the ideal host for Na deposition. Through rational structural design, the composite skeletons with "gradient sodiophilic" properties can be constructed to improve the stability of Na metal anodes during cycling. For example, the "bottom-up" pattern of Na deposition can be achieved by introducing sodiophilic components at the bottom of the skeleton, which can reduce the formation of Na dendrites and improve space utilization within the skeletons [91]. The sodiophilic metals and carbon-based skeletons work together to improve deposition behavior, nucleation patterns, and growth processes. Therefore, the full-featured 3D composite framework is conducive to the realization of the long-term cycling stability of Na metal anodes.

Due to the high Na^+ concentration and low transmission resistance, Na plating usually starts on the top surface of the conventional 3D conductive skeleton, denoted as "top-growth". This phenomenon would hinder the diffusion of Na^+ to the lower part of the scaffold, leading to the formation of Na dendrites and "dead Na" [19]. New 3D sodiophilic gradient frameworks constructed by sputtering Au and Ag nanoparticles at the bottom of 3D carbon foam promoted the "bottom-up growth" of Na metal [136, 137]. However, when the bottom sodiophilic layer is completely covered, Na^+ will continue to preferentially accept electrons at the top of the skeleton. The combination of "gradient

sodiphilicity" and "gradient conductivity" could be more efficient to prevent the "top-growth" of Na in the initial stage. Li et al. investigated a series of scaffolds (conductors vs. insulators) with different coated metals (favorable vs. unfavorable for Na deposition), revealing the deposition behavior of Na on these bottom-coated substrates [138]. When using the conductive matrix (e.g., Cu foam) with sodiophilic metal bottom coating (e.g., Sn), Na would deposit on the top side and form dendrites due to the high conductivity of Cu foam and the slow kinetics of Na transport (Fig. 7(a)). In contrast, when the matrix (e.g., PAN) was insulative, Na deposited nucleate at the bottom of the substrate and grew from bottom to top. This uniform Na deposition was attributed to the synergistic effect of the suitable location and direction of Na deposition and the uniform distribution of Na^+ mediated by the sodiophilicity of PAN. Moreover, only guided layers like Sn and Au (which have advantages for Na deposition) could control the Na deposition location, thus improving the negative electrode performance of Na. The PAN/Sn substrate achieved high Coulomb efficiency of over 99.5% in Na plating/stripping cycling at a high current density of 5 mA·cm^{-2} with the capacity limitation of 10 mAh·cm^{-2} and stable operation of more than 2500 h in symmetric cells at 2 mA·cm^{-2}.

In addition to metal, metal compounds can contribute to the sodiophilicity of the hybrid carbon matrix and reduce the reaction energy barrier to enhance the Na deposition kinetics. Sodiophilic metal compounds can be divided into nonreactive and reactive metals [109, 139]. The nonreactive species have excellent chemical stability, which can maintain stable crystalline structure during the whole charge and discharge process. For example, the multichannel carbon nanofibers embedded with ultrafine MoN catalyst (MoN@CNFs) could be used as a dual-function host material for sulfur cathode and Na metal anode in advanced RT Na-sulfur batteries (Fig. 7(b)) [140]. The binding energies of MoN and graphite with Na are −0.88 and 0.44 eV, respectively, demonstrating MoN can chemically attract Na atoms and induce their uniform deposition process. In addition, COMSOL Multiphysics and finite element method were used to simulate the distribution of Na^+ around the Na/MoN@CNFs anode (Fig. 7(c)). A small Na^+ concentration gradient difference was identified near the surface of Na/MoN@CNFs, indicating that the Na/MoN@CNFs had low concentration polarization during Na deposition, thus avoiding the formation of Na dendrites. The RT Na-sulfur battery with Na/MoN@CNFs anodes showed excellent discharge performance (990 mAh·g^{-1} at 0.2 A·g^{-1} after 100 cycles) and a long life of over 1500 cycles at 2 A·g^{-1}. Besides, the MoN catalyst can maintain a stable crystalline phase during charge and discharge process, demonstrating its excellent stability. In contrast, the reactive species can spontaneously react with Na metal to form

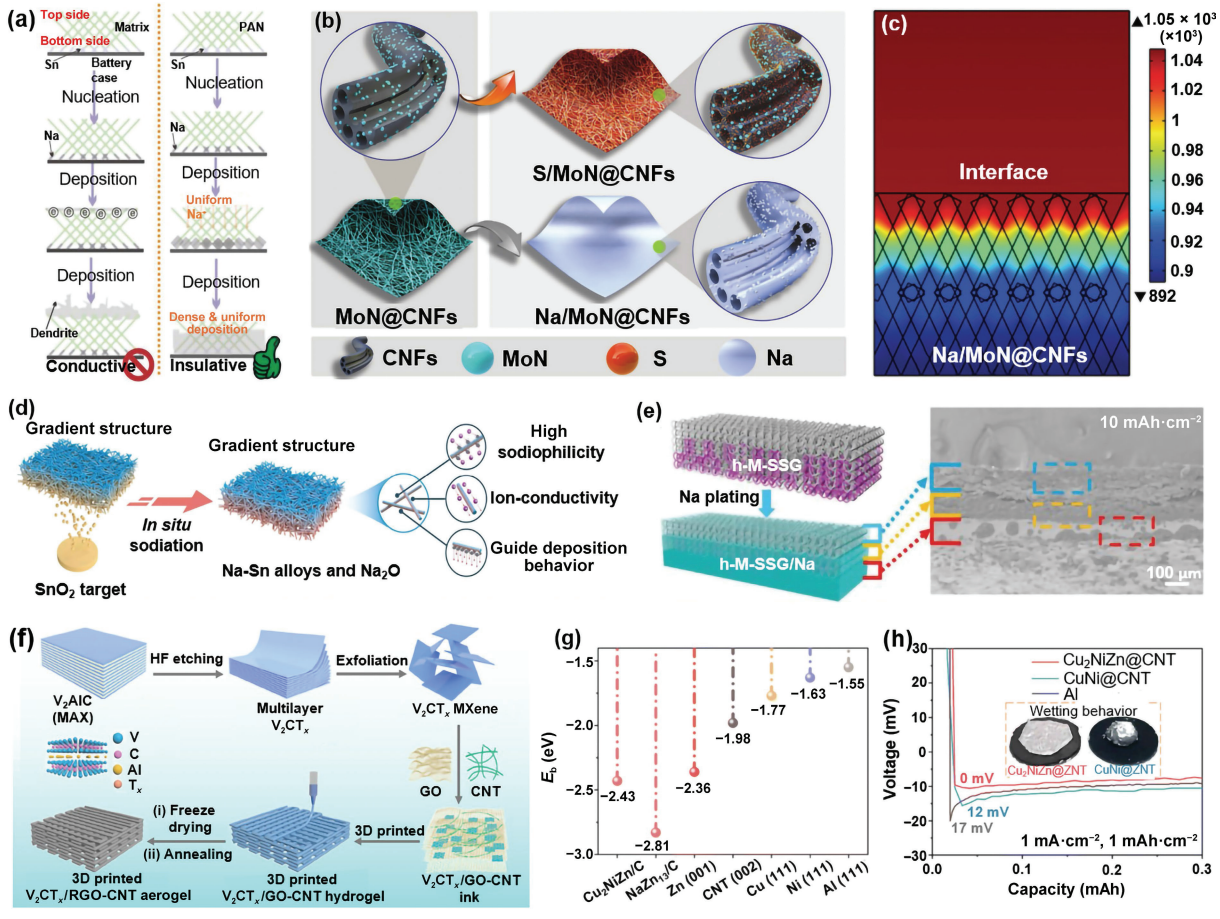

Figure 7 (a) The schematics of Na deposition on the Sn bottom coated conductive and insulative matrix, respectively. Reproduced with permission from Ref. [138], © Wiley-VCH GmbH 2020. (b) Synthesis schematic for the S/MoN@CNFs cathode and the Na/MoN@CNFs anode. (c) Na^+ concentration distribution by the finite element simulation for the Na/MoN@CNFs anode. Reproduced with permission from Ref. [140], © Wiley-VCH GmbH 2022. (d) Schematic illustration for the fabrication of 3D SnO_2-CNFs scaffold and further sodiation process. Reproduced with permission from Ref. [142], © Elsevier Ltd. 2022. (e) Illustration of Na deposition on h-M-SSG and corresponding optical photographs of the top and bottom of h-M-SSG before and after Na plating (left). Cross-sectional SEM images of h-M-SSG after Na deposition with 10.0 mAh·cm^{-2} (right). Reproduced with permission from Ref. [151], © Wiley-VCH GmbH 2022. (f) Schematic diagram of the preparation process of a 3D-printed V_2CT_x/RGO-CNT microgrid aerogel electrode. Reproduced with permission from Ref. [152], © American Chemical Society 2022. (g) Binding energies of Na onto the dominant crystalline planes of different models. (h) Nucleation overpotentials of the Cu_2NiZn@CNT, CuNi@CNT, and Al foil substrates at 1 mA·cm^{-2}. The inset shows the wetting behaviors of the Cu_2NiZn@CNT and CuNi@CNT film towards molten Na. Reproduced with permission from Ref. [153], © The Royal Society of Chemistry 2022.

sodiophilic alloys with enhanced sodiophilic properties and inorganics with high Young's modulus to improve the stability of SEI layers [141]. Xie et al. modified CNF scaffolds by magnetron sputtering SnO_2 to prepare 3D gradient sodiophilic scaffold (SnO_2-CNFs) [142]. The elemental mapping showed that the contents of Sn and O elements increased gradually from top to bottom, which proved that SnO_2 concentration gradient existed on the CNFs scaffold. The higher SnO_2 content led to preferential deposition of Na to the bottom of the scaffold and achieved a "bottom-up" deposition pattern. During the initial cycle, SnO_2 reacts Na to generate Na-Sn alloy and Na_2O (i.e., $4Na + SnO_2 = 2Na_2O + Sn$ and $Sn + xNa = Na_xSn$, $0 \le x \le 3.75$), which contribute to the stable SEI and homogeneous Na nucleation and deposition (Fig. 7(d)). After stripping, only a small amount of Na remained on the top surface of SnO_2-CNFs scaffold, which was conducive to improving CE. Therefore, the electrode showed excellent electrochemical reversibility, stability, and cycle life, with CE up to 99.88% after 1500 cycles (3000 h) at 3 $mA·cm^{-2}$ and 3 $mAh·cm^{-2}$.

MXene is an emerging two-dimensional (2D) transition metal carbide/nitride with high conductivity, abundant functional groups, good hydrophilicity, and high mechanical modulus [143]. The sodiophilic function groups (e.g., –O and –F) on the surface of MXene play important roles in reducing nucleation overpotential and inducing uniform Na nucleation [144]. Moreover, MXene has high electron and ion transport dynamics due to its high electronic conductivity and open cross-linked network. Therefore, MXene can be used as a promising substrate for Na deposition [145]. However, the inevitable self-restacking of pristine MXene nanosheets reduces the porosity of MXene-based scaffold [146]. Through elaborate structure design, the composite skeleton formed by MXene and carbon-based materials can serve as a promising substrate for Na deposition [147]. Among many kinds of MXene, Ti_3C_2 is the most common and widely used material in battery research [148–150]. Chen et al. designed a novel lightweight scaffold with stepped sodiophilic gradient structure (h-M-SSG) [151]. The 2D layered Ti_3C_2 was alkalized and recombined to form one-dimensional (1D) fibrous and hydroxylated Ti_3C_2 (h-Ti_3C_2). Different contents of h-Ti_3C_2 were then mixed with CNT in solution. Finally, h-M-SSG was prepared by vacuum filtration, in which the content of h-Ti_3C_2 increased gradually from the top to the bottom. The h-Ti_3C_2 contains abundant O, F, and K functional groups. The O and F functional groups have larger binding energy with Na atoms, which can effectively reduce the nucleation energy. The K functional group can be alloyed with Na, which further improves the sodiophilic properties. The h-Ti_3C_2 would guide bottom-up deposition of Na (Fig. 7(e)). SEM images of h-M-SSG after Na deposition showed clear stratified structure. Stepped sodiophilic gradient structure can effectively enhance the affordability of h-M-SSG for high current density and capacity. The Na-O_2 battery based on h-M-SSG/Na still had excellent capacity and rate performance with a potential difference of 0.137 V after 45 cycles between 1000 $mA·g^{-1}$ (equivalent to 0.14 $mA·cm^{-2}$) and 1000 $mAh·g^{-1}$ (equivalent to 0.14 $mAh·cm^{-2}$). V_2CT_x MXene also shows high electrochemical activity and good ionic conductivity, which is suitable for Na metal substrate. Wang's group constructed V_2CT_x/RGO-CNT (RGO = reduced graphene oxide) microgrid aerogel electrode through 3D printing technology (Fig. 7(f)) [152]. Stable layered porous 3D printed structures with large surface area can reduce current density. Abundant sodiophilic functional groups of V_2CT_x provided a large number of Na nucleation active centers. CNT and RGO not only improved the mechanical stability of the scaffold to support V_2CT_x MXene, but also accelerated charge transfer. Due to the above advantages, the manufacturing of MXene matrices by advanced 3D printing technology improved the cyclic stability of Na metal anodes.

Currently, many studies on Na metal anodes have pre-stored excess Na, which reduces the energy density of Na metal batteries. The anode-free Na metal batteries may significantly increase the energy density. However, it is difficult to achieve reversible Na utilization when the Na reservoir is limited. Ma et al. prepared a lightweight (1.0–1.2 $mg·cm^{-2}$) and flexible Na deposition substrate by confining sodiophilic Zn-containing multialloys (from ternary to medium/high entropy alloys, MEAs/HEAs) to CNT scaffolds [153]. The alloying of Na-Zn produced heterogeneous $NaZn_{13}$ substances that were uniformly distributed in CNT. $NaZn_{13}$ would promote uniform Na nucleation and guide transverse Na propagation. Through modeling and DFT calculation (Fig. 7(g)), Cu_2NiZn (111)/C and $NaZn_{13}$ (422)/C models showed higher enhanced binding energy (E_b) for Na adsorption, which was ~ 2.43 and ~ 2.81 eV, respectively. The Cu_2NiZn@CNT substrate exhibits excellent wettability to molten Na due to the increased sodiation activity of the Zn species. In addition, zero nucleation overpotential (0 mV) of Cu_2NiZn@CNT substrate was observed at 1 $mA·cm^{-2}$ (Fig. 7(h)). A soft pack battery composed of the presodiated Cu_2NiZn@CNT substrate (0.2 × excess Na) and the $NaVPO_4F$ cathode could simultaneously achieve a weight energy density of 351.6 $Wh·kg^{-1}$ at the maximum power output of 1335.5 $W·kg^{-1}$ (based on the calculation of electroactive materials), and stable cycling durability (93.7% for 200 cycles at 0.5 C), even in geometric bending scenarios.

Due to the large specific surface area, 3D current collectors can be used as excellent hosts for Na deposition. However, the high weight of the metal and the poor wettability of the carbon material to Na metal limit their electrochemical performance. The composite frameworks have various structures that enable dendritic-free Na deposition. Designing a gradient sodiophilic framework structure by adjusting the distribution of sodiophilic sites can effectively prevent the accumulation of Na on the top surface of the skeleton, and greatly improve the stability of long-term cycling performance of Na metal anodes. Unfortunately, complex structural designs hinder the practical application of these advanced composite current collectors. Therefore, more advanced manufacturing techniques need to be explored to simplify the preparation process. Finally, various 3D collector designs were summarized and compared in terms of overpotential, current density, plating/stripping capacity, and lifespan (Table 2).

4 Strategies for regulating sodium deposition kinetics

Researchers generally believe that the main causes of Na dendrite formation are random Na^+ diffusion behavior and slow surface atomic diffusion. Under the condition of constant deposition current, the insufficient diffusion rate of Na ions/atoms leads to uneven Na^+ flux. Affected by the surface morphology and electric field distribution of the anode, Na^+ in local high concentration produces aggregation and nucleation. In addition, the high surface diffusion barrier causes the lateral diffusion rate to be lower than the vertical local deposition rate. Na^+ preferentially tends to deposit at the tip, thus causing the growth of Na dendrites [41, 154]. Therefore, it seems to be a more direct method to regulate Na diffusion behavior by electrochemical method. In this section, alloy layers, nanoscale "sodiophilic seeds", and single metal atoms are presented to enhance Na ions/atoms dynamics.

4.1 Sodium alloy layer

Na metal alloy has naturally high Na^+ diffusion coefficients, which can serve as regulators to accelerate Na interfacial diffusion kinetics and inhibit dendrite growth [155, 156]. However, adding a

Table 2 Comparisons of the overpotentials of the reported pretreated electrodes[a]

Electrode	Overpotential (mV)	Current density (mA·cm^{-2})	Capacity (mAh·cm^{-2})	Lifespan	References
Na@O-CF	50	0.5	1	400 h	[107]
CF@ZnO/Na	25	1	1	300 cycles	[111]
Na_2Se/Cu@Na	70	1	1	500 h	[112]
Cu/Zn/SnO_2 @Na	25	1	1	820 h	[113]
Na/SMO	20.8	5	5	500 cycles	[114]
NSCA-31	50	1	1	700 h	[115]
Na/NaSn	24.5	1	4	1600 h	[117]
Na/L700	< 50	1	0.5	1000 h	[123]
SCNF@Na	~ 40	1	1	2700 h	[125]
LCNF@Na	50	0.5	0.5	790 h	[126]
Na-O-CCF	5.3	10	1	700 h	[127]
ONCNFs-Na	22	4	2	500 h	[130]
Na@OCF	25	2	1	3000 h	[131]
Na@C_FN-CP	16	1	1	2100 h	[133]
CMFS@Na	12	5	5	1000 cycles	[135]
Na-PAN/Sn	20	2	2	2500 h	[138]
MoS_2@NCF/Na	30	6	3	3000 cycles	[139]
Na/MoN@CNFs	35	1	1	1300 h	[140]
$SnCl_4$@ Na-RGO	100	2	2	500 h	[141]
SnO_2-CNFs@Na	45	5	5	1500 h	[142]
Ti_3C_2 MXene@g-C_3N_4@Na	11	1	1	700 h	[146]
Na-$Ti_3C_2T_x$-CC	20	5	1	300 h	[148]
C-NTO-3/Na	77.5	5	20	320 h	[149]
h-M-SSG/Na	93	10	10	100 h	[151]
Na@V_2CT_x/RGO-CNT	9.6	0.5	0.5	1700 cycles	[152]
Cu_2NiZn@CNT	~ 22	2	2	800 h	[153]

[a]SMO = Sb_2MoO_6; NSCA = Na/SnO_2 composite anode; LCNF = lignin-derived carbon nanofiber; OCF = oxygen-doped carbon foam; NCF = N-doped carbon nanofibers; CC = carbon cloth; and C-NTO = 1D/2D $Na_3Ti_5O_{12}$-MXene hybrid nanoarchitecture.

large content of alloys will dramatically decrease the battery energy density and aggravate the anode volume fluctuation [157]. These problems can be avoided by making the alloy a thin surface coating without compromising its positive effect on regulating Na deposition behavior. The typical passivation SEI layer is electronically isolated and affects the rate of Na deposition. In contrast, the alloy layer allows for rapid diffusion of Na^+ and uniform Na^+ flux. Therefore, Na metal anodes with alloy surface coating exhibit good high-rate performance. In addition, thin metal coatings can be prepared by magnetron sputtered and vapor deposition on the planar substrate. Thermodynamic and ion transport studies have demonstrated that the alloying reactions of these metals with Na at room temperature help to anchor Na firmly to the planar substrate [158].

To avoid phase aggregation when two metals are simply mixed, the synthesis method based on spontaneous reaction is undoubtedly feasible. Archer's group added SnTFSI solution to the surface of the Li metal, which formed a Sn coating by ion-exchange chemistry. Then the Sn-Na mixed electrode was prepared in a similar way [159]. Due to the high reactivity of Na, the Sn layer on the Na metal anode mainly existed in the form of Na-rich alloys rather than metals. At a moderate current density (0.25 mAh·cm^{-2}), the symmetrical cell with Sn-Na electrodes could operate stably for over 1600 h without signs of voltage divergence. Besides, the surface of Na metal can be modified by SbF_3-DMC solution through spontaneous displacement reaction and subsequent alloying reaction (i.e., 3Na + SbF_3 = 3NaF + Sb and Sb + 3Na = Na_3Sb) [160]. The X-ray diffraction (XRD) curve showed that the longer the treatment time, the more Na_3Sb alloy was formed in the protective layer (Fig. 8(a)). The protective layer had a multiple structure, the upper layer was the compact SEI with rich NaF, and the inner layer was dominated by Na_3Sb alloy (Fig. 8(b)). Due to the synergistic action of multiple components, this reinforced concrete-like composite interfacial layer also exhibited ultra-low interfacial impedance and ultra-strong mechanical strength, which could inhibit the formation of Na dendrites.

Gas phase reactions usually have faster reaction rates than liquid phase reactions. By allowing Na metal to react with $SnCl_4$ vapor, a metal alloy interface (MAI) containing Na-Sn alloy (Na_xSn_y) could be formed immediately (~ 10 s) on the Na metal surface [161]. The MAI has four important properties, strong electrode adhesion, high ionic conductivity (0.22 mS·cm^{-1}), high Young's modulus (21.2 GPa), and low electrolyte permeability. Thus, a Na anode with MAI could cycle over 650 cycles at 2 mA·cm^{-2} in a symmetric cell without short-circuiting, showing stability even at the high current density of 7 mA·cm^{-2}. The Na diffusion behavior of Na-Sn alloy ($Na_{1.17}Sn_2$) was investigated by DFT calculations (Fig. 8(c)). It was shown that the diffusion barriers of 6 → 4' (~ 0.11 eV) and 3 → 1' (~ 0.46 eV) along the path were determined to be low, as shown in Fig. 8(d). This is attributed to the small Na-Na repulsion along the diffusion channel due to the nearby vacancy defect (*). In addition, the Na

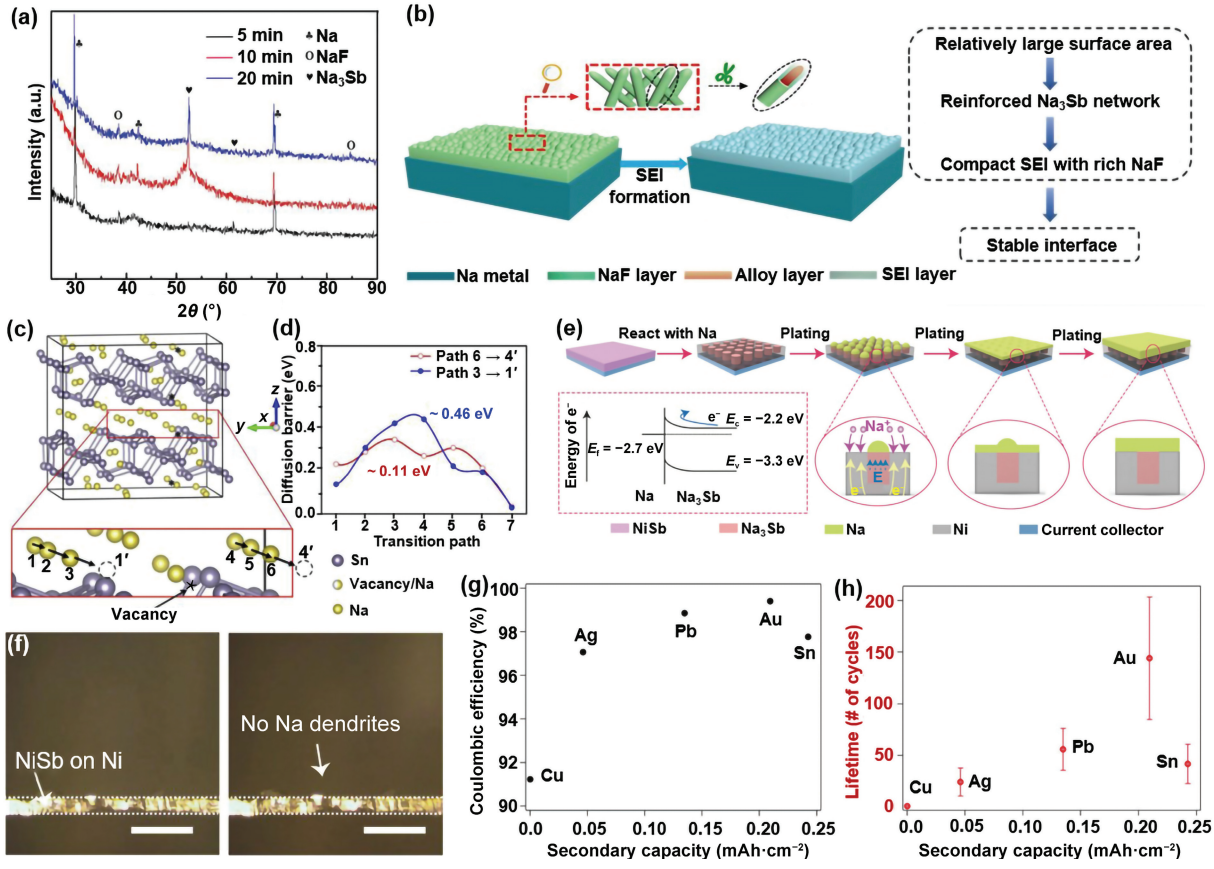

Figure 8 (a) The XRD of sodium-alloy-fluoride (SAF-Na) with different processing time. (b) The schematic of speculated protective mechanism of SAF-Na. Reproduced with permission from Ref. [160], © WILEY-VCH Verlag GmbH & Co. KGaA, Weinheim 2019. (c) Model structure of $Na_{1.17}Sn_2$ with vacancy defect (*), arrows in the magnified view represent possible diffusion paths for Na (e.g., path 6 → 4' indicates a vacancy is created at site 4' first and Na moves from site 6 to 4'). (d) Theoretically predicted diffusion barrier for Na along paths 6 → 4' and 3 → 1'. Reproduced with permission from Ref. [161], © Elsevier B.V. 2020. (e) Schematic illustration of the smoothing deposition by the self-regulating mechanism. (f) *Operando* observation of the Na plating on a NiSb-coated current collector (scale bar: 100 μm). Reproduced with permission from Ref. [162], © Wiley-VCH GmbH 2021. Anode reversibility and long-term cycling results, (g) CE and (h) lifespan plotted again reversible secondary capacity of various counter electrode materials. Reproduced with permission from Ref. [163], © Wiley-VCH GmbH 2022.

vacancy formation energy (E_f) was calculated to be about 1.1 eV. This indicated that Na vacancies formed relatively easily, thus facilitating Na diffusion in the structure.

Random Na^+ behavior can be induced to produce uniform Na deposition by adjusting the electric field distribution near the interface of Na anode. Zheng et al. reported a self-regulating alloy interface using nickel-antimony (NiSb) alloy [162]. During the electroplating process, Na^+ reacted with NiSb interface to form Na_3Sb alloy and Ni metal. Semiconductor Na_3Sb nanoislands were chemically sodiophilic yet electron hindered, while the conductive Ni matrix was sodiophobic but electron-favored conductive. The internal electric field of Na/Na_3Sb heterostructure inhibited the subsequent growth of Na seeds. The Na metal was then deposited on the surface of the Ni matrix, which connected the nanoseeds and flattened the Na metal deposition layers (Fig. 8(e)). This unique self-regulation mechanism could effectively inhibit dendrite growth. The morphologic evolution of Na metal on NiSb modified collector was recorded by *in situ* optical microscope (Fig. 8(f)). The surface of the NiSb modified collector remained smooth and no dendrites were observed throughout the electrochemical deposition process.

The strength of alloying and the thickness of the alloy layer may affect the properties of Na metal anodes. Archer et al. investigated Na alloying capabilities with various coating materials (Ag, Pb, Au, and Sn) [163]. Although Sn and Pb were more sodiophilic, Au showed the best reversibility for Na plating/stripping (as measured by CE) (Fig. 8(g)). This is due to the complex alloying/dealloying process of Na-Sn and Na-Pb (the Na-Sn alloying phase with the highest possible Na content is Sn_4Na_{15}, while for Na-Pb it is Pb_4Na_{15}), resulting in poor reversibility. In contrast, in the Na-Au system, one Au atom alloys with only two Na atoms, showing great stability. The volume change during the alloying/dealloying process eventually leads to the mechanical failure of the coating. Because of the smaller volume change caused by Na-Au, the alloying interface was more robust. Therefore, the Au coating had better cycling stability (Fig. 8(h)). Moreover, the thickness of the coating layer also affected the cycling performance of Na metal anodes. The thickness of the coating layer in the range of 50–100 nm generally yielded the best CE and life span. If the coating layer was too thick or too thin, it might be crushed or delaminated under large volume changes. Thus, the Au coating layer (~ 100 nm thick) resulted in the highest reversibility in the range of 1 to 5 $mAh·cm^{-2}$.

The alloy coating layer not only improves the affinity of the anode surface to Na, but also promotes the rapid diffusion rate of Na ion/atom at the interface. However, repeated alloying and dealloying may cause cracking and peeling of the sodiophilic layer. Different thicknesses and alloying strengths will affect the stability of the alloy layer, but little attention has been paid to this aspect. Moreover, most studies have not explored the internal transport mechanism of Na in the alloy layer. These factors limit the application of alloy layers on high-rate Na metal anodes.

4.2 Sodiophilic nanoscale particles

Metal NPs are already an important class of catalysts, which are widely used in heterogeneous catalysis, sensors, batteries, etc.

[164]. Sodiophilic NPs can act as "seeds" to guide Na nucleation and growth, alleviating volume changes and avoiding extra weight increase [165]. NPs can be embedded in 2D current collectors or 3D frame structures in flexible manners. By controlling the position and number of "seeds", the nucleation and growth behavior of Na can be guided, enabling dendritic-free Na deposition [142]. These metal NPs formed sodiophilic phases by *in situ* alloying, which reduces the nucleation and diffusion barriers of Na. Moreover, the small size of the NPs makes them more efficient than the alloy layer. Therefore, sodiophilic NPs can be used as catalysts to achieve high-performance Na metal anodes.

The inorganic layer with high ionic conductivity and Young's modulus limits the growth of Na dendrites, but its limited mechanical strength and sodiophilicity cannot achieve long-term cycling stability. Previous reports have shown that implantation of sodiophilic NPs on planar substrate is conducive to smooth Na deposition [114, 166]. Yu's group reported a heterogeneous interfacial layer composed of metallic vanadium (V) and Na_2S nanophases [167]. In the process of Na deposition, as the adsorption sites, V metal preferentially adsorbed Na^+. Then the Na_2S with high ionic conductivity facilitated Na^+ pass through the interface layer. Finally, Na^+ captured electrons to form Na nuclei, which then grew uniformly on the anode surface (Fig. 9(a)). The exchange current density of Na_2S/V/Na is 0.569 mA·cm^{-2}, which was much higher than those of bare Na (0.014 mA·cm^{-2}) and Na_2S/Na (0.054 mA·cm^{-2}), indicating that the charge transfer ability of the Na_2S/V mixed interface layer was improved (Fig. 9(b)). The activation energies of Na_2S/Na and Na_2S/V/Na electrodes decreased from 49.15 to 43.28 and 36.09 kJ·mol^{-1}, respectively. It was shown that the Na_2S/V mixed interface layer promoted the rapid diffusion of Na^+ through the SEI layer (Fig. 9(c)). Therefore, the Na_2S/V protective layer can effectively inhibit the growth of Na dendrites and form a flat and smooth deposition morphology. Later, the same group prepared a multiphase interface consisting of Na_2Se and metal V by reacting VSe_2 with Na metal, which also showed excellent performance [168].

During the cycling process, the metal NPs may aggregate and thus reduce the reversibility [169]. The carbon shell coating can effectively avoid the occurrence of such phenomenon [170, 171]. Lee et al. reported a 3D nanostructured porous carbon particle containing carbon-shell-coated Fe NPs (PC-CFe) as a highly reversible subject to control the growth of Na metal [172]. The PC-CFe has a unique 3D hierarchical structure based on sub-micrometer-sized carbon particles, ordered open channels, and uniformly distributed CFes on the surface (Fig. 9(d)). In order to evaluate the effect of carbon coatings on Fe NPs on the enhancement of sodiophilicity, DFT calculations of the Na adsorption energy on Cu (111), Gr, and CFes were performed. In addition to the pristine graphene surface (P-Gr), various point defects such as monovacancy (MV), divacancy (DV), trivacancy (TV), and Stone–Wales (SW) defects were considered. The adsorption energy of Na in P-Gr layer was 0.56 eV, which indicated that Na nucleation on P-Gr layer was energetically unfavorable. However, in the case of CFe, the adsorption energy of Na on P-CFe surface was significantly enhanced to −2.54 eV. It was worth noting that in the CFe system, there was a good correlation between the adsorption energy of Na and the amount of charge (electron) transfer of Fe atoms (Fig. 9(e)), indicating that

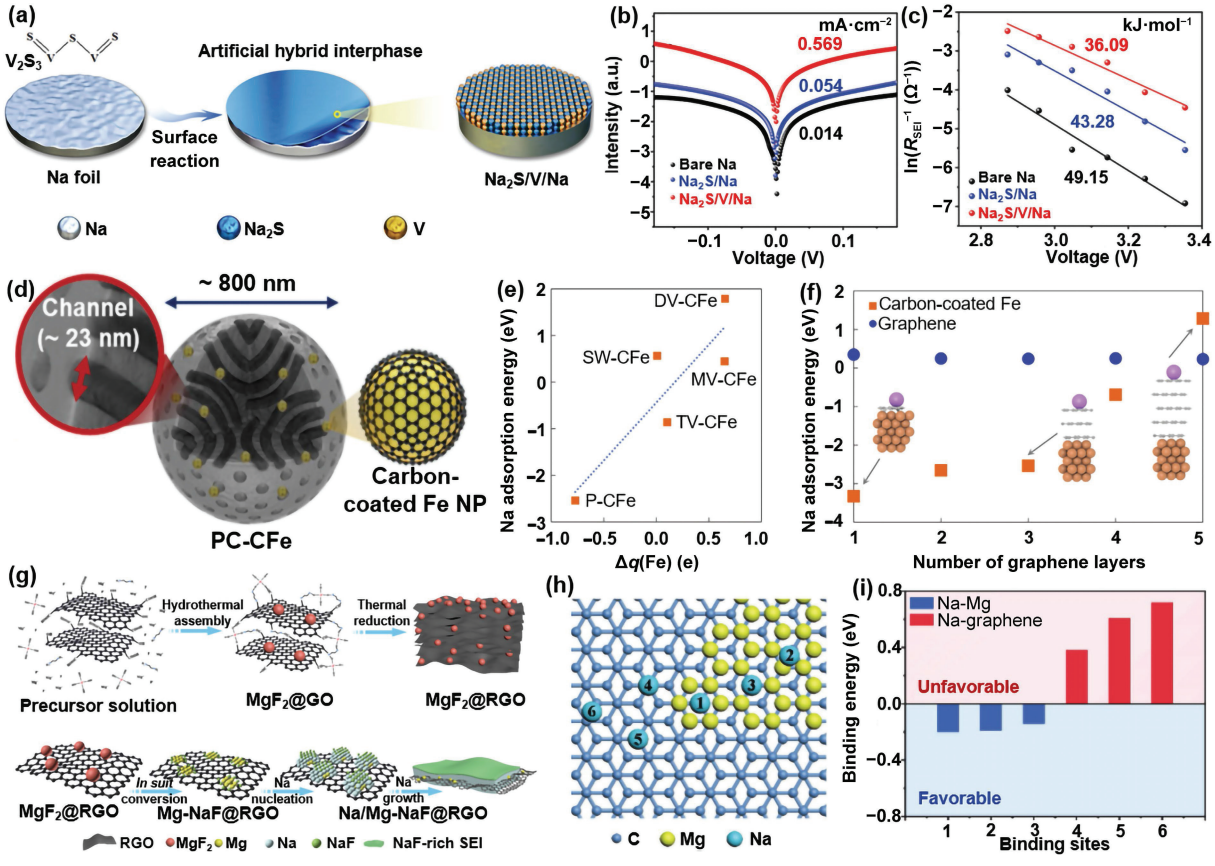

Figure 9 (a) Illustration of the synthesis of Na_2S (K_2S)/V/Na. (b) Tafel profile obtained from cyclic voltammetry measurements after 30 cycles at 1 mA·cm^{-2} and 1 mAh·cm^{-2}. (c) The activation energy (E_a) of Na^+ diffusion through the SEI layers. Reproduced with permission from Ref. [167], © Wiley-VCH GmbH 2022. (d) Schematic illustration of PC-CFe. (e) Na adsorption energy as a function of Bader charge (electron) difference of Fe atoms before and after Na adsorption. A negative value for Δq(Fe) indicates the electron donation of Fe atoms. The dashed line is a guide for the eye. (f) Na adsorption energy on graphene and carbon-coated Fe as a function of the number of carbon layers. Reproduced with permission from Ref. [172], © Wiley-VCH GmbH 2022. (g) Illustration of the synthesis of the MgF_2@RGO aerogel and the working mechanism of MgF_2@RGO aerogel as a host material for Na metal anodes. (h) Illustration of the binding sites for Na on the Mg/graphene surfaces and (i) corresponding binding energies based on the DFT calculations. Reproduced with permission from Ref. [175], © Zhao, L. F. et al. 2022.

the Fe atoms underneath the carbon layer played a decisive role in the Na adsorption energy. The thickness of carbon layer in the CFe system also had an effect on the Na adsorption energy (Fig. 9(f)). Strong Na adsorption on carbon coated Fe is maintained up to three carbon layers (~ 1 nm), but decreases sharply beyond four carbon layers. Moreover, in the absence of Fe atoms, the thickness of carbon layer did not affect the Na adsorption. These results suggest that carbon-coated Fe NPs may regulate Na nucleation behavior by improving their sodiophilicity. Moreover, porous carbon particles with large surface areas and regular surface structures are particularly conducive to uniform distribution of electric fields, which can prevent Na dendrite growth.

The classical Chazalviel's diffusion model states that dendrite growth begins at "sand time" (τ). At the time τ, the ion concentration near the anode decreases to zero and dendrites start to appear. Reducing the effective current density or increasing ion mobility can delay the dendrite appearance [173]. To this end, the combination of 3D porous frameworks with nanoscale sodiophilic seeds was applied to dendrite-free Na metal anodes [169, 174]. Dou et al. developed a strong MgF_2@RGO aerogel as a multifunctional material for Na metal cathode [175]. MgF_2 nanocrystals could be converted to Mg (nucleation site) and NaF (solid electrolyte interface) during the initial stage of the first Na plating (Fig. 9(g)). DFT calculations were used to determine the corresponding binding energies of Na at each binding site at the (101) plane of Mg and the graphene plane of RGO (Figs. 9(h) and 9(i)). The binding energies of the graphene layer are 0.38, 0.61, and 0.72 eV, so that the graphene layer is not conducive to Na deposition. The binding energies of Na adsorbed on Mg were −0.20, −0.19, and −0.14 eV, indicating that the surface of Mg was favorable for Na adsorption. Sodiophilic Mg seeds ensure uniform Na nucleation and growth. As a result, the Na/MgF_2@RGO electrode could stabilize the cycling performance for over 1600 h, more than twice as long as the Na/RGO electrode.

From the thermodynamic point of view, metals with certain solubility in Na can significantly reduce the nucleation barrier and thus improve the deposition behavior of Na [176, 177]. However, the following problems remain in the application of metal NPs in the protection of Na metal anodes: (1) The distribution of sodiophilic seeds is crucial for uniform Na nucleation. How to achieve maximum dispersion of active sites without particle agglomeration is essential. (2) Due to the mechanical stress caused by the volume change during alloying/dealloying processes, strong adhesion is required to maintain the NPs on the substrates during cycling. (3) Direct exposure of alloy species to electrolyte will increase irreversible Na^+ consumption, therefore proper spatial arrangement of sodiophilic materials is critical but challenging for stable interfacial properties and structural integrity of the deposition substrate. (4) It remains difficult to determine the underlying physicochemical factors that determine the relative affinity of Na to the intermediate alloy. (5) The unsaturated coordination atoms on the surface of NPs are often the active sites for catalysis. In the process of catalytic reaction, only a few active components play a catalytic role, resulting in low utilization rate of active materials.

4.3 Single atom catalysts (SACs)

SACs are specially supported metal catalysts, which refer to the uniform distribution of metals on the carrier in the form of single atoms. There are no homoatomic metal–metal bonds [178]. When the particle dispersion reaches the size of an individual atom, many new properties appear, such as sharply increasing surface free energy, quantum size effect, interaction between unsaturated coordination environment, and metal carrier. These unique characteristics are conducive to the improvement of the catalytic effect. Since each metal atom is an individual active site, an atomic utilization efficiency close to 100% can be achieved [179, 180]. In addition, single atomic sites have more defined and uniform active centers than nanoparticles, which is conducive to the study of structure-property relationships. Therefore, SACs show great potential for implementing high-performance Na metal anodes.

SACs were first applied to Na metal anodes in 2019. Yan et al. designed a carbon-substrate-supported nitrogen-anchored Zn single atoms (Zn_{SA}-N-C) as a current collector [181]. The transmission electron microscopy (TEM) image showed that all Zn species existed only as isolated individual atoms (circled in yellow), and neither nanoparticles nor clusters were detected (Fig. 10(a)). The single Zn modified electrode could not only significantly reduce the nucleation barriers of Na (basically zero nucleation overpotential), but also fully improve the utilization rate of Na in the cycling process. The full cell composed of Na-Zn_{SA}-N-C anode with finite Na source and $Na_3V_2(PO_4)_3$ cathode had a stable cycling performance of over 1000 cycles and a high CE of nearly 100%. The utilization rate of Na reached an astonishing nearly 100%.

Compared with non-metallic atom and nano-cluster doping, metal single atom doping can enhance the interaction between the electroplating matrix and Na atoms more efficiently. Li and colleagues investigated the nucleation and growth behavior of Na on the flat graphene substrates with different heteroatomic dopants, including boron (B) and N. The experimental results revealed a binding-energy-dominated Na nucleation-growth pattern [182]. The binding energy of Na calculated by DFT decreased in the order of B-doped graphene (1.9 eV) > N-doped graphene (1.4 eV) > bare copper (1.2 eV) > pristine graphene (0.95 eV). Thus, B-doped graphene exhibited the lowest nucleation overpotential at current densities of 0.5 to 5 $mA{\cdot}cm^{-2}$ (Fig. 10(b)). In another work, Liu et al. demonstrated that the Co single atomic sites exhibited stronger sodiophilicity than Co NPs [183]. The adsorption energy of Na^+ on the Co (111) surface of Co NPs was −1.33 eV, while it dropped to −2.29 eV at Co single atom sites in Co_{SA}@NC. Thus, Co_{SA}@NC substrate exhibited the lowest Na nucleation overpotential (all less than 15.0 mV), when the current density increased from 0.5 to 5.0 $mA{\cdot}cm^{-2}$ (Fig. 10(c)). In addition, the Na-Co_{SA}@NC electrode could maintain a high CE of 99.95% for 850 cycles, and the polarization of Na metal anode was limited to 20 mV, with an extremely long cycle life (> 2000 h) at 1.0 $mA{\cdot}cm^{-2}$.

The rare-earth metal yttrium (Y)-N_4 unit features favorable sodiophilic and sulfurophilic Janus properties, which can be used as the host of high-performance Na metal anode and sulfur cathode in Na-S battery. Li et al. simulated the molecular dynamics (MD) of the entire growth process of Na dendrites on NC and YN_4/C surfaces by high-dimensional neural network potentials (HDNNPs) based on first principles [184]. The simulation began with some sparsely distributed Na atoms, and the subsequent Na atoms immediately spread out to the NC and YN_4/C models at an identical rate (Fig. 10(d)). The Na clusters did not generate even at 500 ps on YN_4/C, while on NC, which formed as early as 300 ps. This indicates that YN_4 can trap Na atoms as nucleating seeds and further hinder the free movement of other Na atoms through steric effect, which is conducive to uniform metal deposition rather than local aggregation. The charge density difference analysis results showed that the interaction between Na^+ and YN_4/C was stronger than that between NC (Figs. 10(e) and 10(f)). Therefore, Na^+ was effectively absorbed on these active sites and synergistically promoted the Na^+ storage performance. As a result, the as-constructed Y

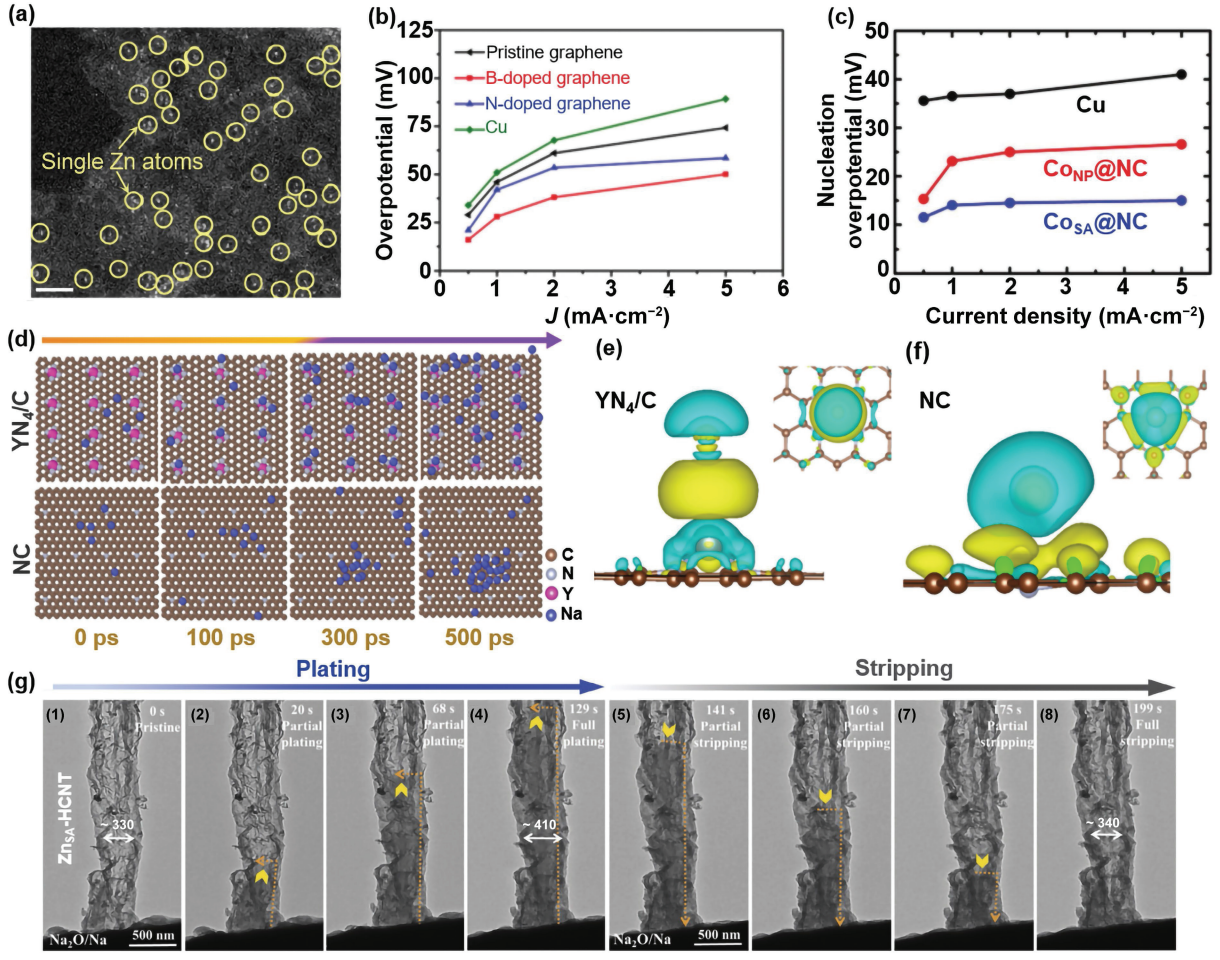

Figure 10 (a) High-angle annular dark-field scanning TEM (HAADF-STEM) image of Zn_{SA}-N-C. Single Zn atoms are highlighted in yellow circles. Scale bar, 2 nm. Reproduced with permission from Ref. [181], © American Chemical Society 2019. (b) Nucleation overpotential versus current density profiles of different substrates. Reproduced with permission from Ref. [182], © WILEY-VCH Verlag GmbH & Co. KGaA, Weinheim 2019. (c) Plots of the nucleation overpotentials of Na on Cu foil, Co_{NP}@NC, and Co_{SA}@NC electrodes as function of current density. Reproduced with permission from Ref. [183], © Wiley-VCH GmbH 2021. (d) Snapshots of molecular dynamic simulations at specific simulation times (t = 0, 100, 300, and 500 ps) of the YN_4/C and NC electrodes. Top and side views for the charge density difference of Na adsorption on the (e) YN_4/C and (f) NC electrodes; the yellow and blue sections represent the electron accumulation and loss regions, respectively. Reproduced with permission from Ref. [184], © American Chemical Society 2022. (g) *In situ* TEM observation of a typical Na plating/stripping cycle on a Zn_{SA}-HCNT. Reproduced with permission from Ref. [185], © Wiley-VCH GmbH 2022.

SAs/NC-S||Y SAs/NC-Na full cell could provide a high capacity of 822 mAh·g^{-1} and achieve a capacity retention rate of 97.5% over 1000 cycles at a high current density of 5 A·g^{-1}.

Most carbon-based skeletons such as CNTs and CNFs store only small amounts of Na in outer space, resulting in a low Na loading at the anode. Reliable sodiophilic doping sites can promote Na^+ infiltration into the tube, and reasonable geometric space can reduce mechanical stress, thus achieving highly reversible Na encapsulation. Dong et al. developed Zn single atom sites embedded in the carbon shell (Zn_{SA}-HCNT; HCNT = hollow CNT) to encapsulate Na metal [185]. Zn_{SA}-HCNT has a high surface area, abundant defects, and enriched Zn single atomic sites in the inner wall. As sodiophilic sites, the enrichment of Zn atoms in the interior makes sodium more inclined to initiate nucleation and growth in the cavity. The electrochemical plating/stripping process of Na metal on Zn_{SA}-HCNT was observed by *in situ* TEM. During plating, metallic Na began to nucleate inside the nanotube in the bottom region in contact with the Na/Na_2O electrode, and then grew along the tube until fully filling (Figs. 10(g)(1)–10(g)(4)). When stripping occurred, the deposited Na gradually receded in the opposite direction until completely stripped (Figs. 10(g)(5)–10(g)(8)). Unlike Zn_{SA}-HCNT, multi-walled CNT (MCNT) failed to encapsulate Na metal due to the lack of attractants to allure Na^+ and porous structures to promote Na^+ diffusion through the shell, resulting in dendrites growth outside the nanotube. More importantly, the morphology of Zn_{SA}-HCNT remained almost unchanged throughout the plating/stripping process without fracture, showing excellent structural/mechanical stability.

SACs attract much attention in heterogeneous catalysis due to their well-defined electronic structure, maximum atomic utilization, and excellent catalytic performance. However, there are few reports on the application of SACs in Na metal anodes, and the research on their effects in improving Na deposition is still in its infancy. In general, the catalytic performance of SACs is closely related to the metal species and the local atomic environment. The molecular understanding of the catalytic effects of SACs on local structure at molecular level during Na deposition process is still unclear. In addition, it is difficult to manufacture stable and high-load SACs because of the high surface energy. Controlling SACs with atomic precision to achieve optimized activity is still elusive. Therefore, the controllable synthesis of SACs needs to be further explored.

5 Summary and prospect

Na metal is one of the most potential anode materials for the next-generation rechargeable battery due to its high theoretical capacity, low redox potential, low cost, and abundant natural distribution.

Unfortunately, the practical application of Na metal anodes still faces many challenges, including unstable SEI, uncontrolled Na dendrite growth, inevitable volume changes, and continuous side reactions with electrolytes. In this review, we systematically summarize and discuss recent studies on high-performance Na metal anodes. The first is to optimize the composition of SEI layers through rational structure design to form a protective layer to enhance their mechanical properties and ionic conductivity. The second is to achieve uniform Na deposition by reducing the local deposition current density via 3D sodiophilic collector. Finally, Na ions/atoms diffusion is regulated by the alloy layer, nanoparticle, and SACs. However, the research on Na metal anodes is still in its infancy. There is still a lack of in-depth theoretical and experimental research. To achieve high-performance Na metal anodes with dendrite-free and long-term cycling stability, the following four areas could be the focus in future research:

(1) Investigating the potential mechanisms of Na nucleation and deposition. Until now, there is still a lack of in-depth understanding of SEI formation and dendrite growth of Na metal anodes. This requires more advanced research methods, such as *in situ* characterization and intelligent simulation techniques. Visual tracking of the Na plating/stripping behavior is helpful to dendrite formation mechanism. For example, *in situ* TEM and SEM can capture the morphologic evolution and dynamic structural changes of the anode surface in real time. In addition, *in situ* XPS can detect the evolution of chemical state and composition during SEI formation. Considering the ultra-high reactivity of Na, advanced cryogenic techniques can ensure the authenticity of the obtained chemical information of the Na metal anode and SEI layers. Moreover, with the development of artificial intelligence, simulation technology provides people with another way of research besides experimentation. In terms of electrochemical dynamics, finite element method and molecular dynamics simulation can describe the effect of atomic diffusion on dendrite formation. By combining *in situ* characterization techniques with computer simulation, the mechanism of Na deposition, dendrite growth, and SEI formation can be fully understood.

(2) Exploring more effective protection methods. Reducing the atomic surface diffusion barrier may effectively suppress the dendrite growth at the very beginning. Compared with alloy layers and nanoparticles, SACs seem to be a more effective method to regulate Na ions/atoms diffusion. Of course, SACs also have some disadvantages. For example, when the metal particles are reduced to the level of monatomic particles, the specific surface area increases sharply, resulting in a rapid increase in the free energy of the metal surface. Then it is easy to form large clusters of agglomeration and coupling during preparation and reaction, thus resulting in catalyst inactivation. Therefore, the role of SACs in improving Na metal anodes performance needs to be fully evaluated. Through more ingenious structural design, the catalytic effect of SACs can be maximized. In addition, combining different strategies could further improve the electrochemical performance of Na metal anodes.

(3) Developing SSEs. Compared with flammable organic liquid electrolytes, SSEs have an absolute advantage in safety. Moreover, the high mechanical strength enabled SSEs to inhibit the growth of Na dendrites. However, low ionic conductivity and high interfacial impedance hinder the application of SSEs in Na metal batteries. In addition, insufficient contact between the SSEs and the Na metal surface result in uneven Na deposition, further deteriorating the interfacial stability. Meanwhile, Na dendrites can grow in the interstitial space due to the uneven composition of SSEs. Therefore, the development of all-solid-state Na metal batteries still needs to be considered in combination with the strategies described above.

(4) Optimize the Na metal anodes in different full batteries. Achieving high-performance Na metal-based full cells requires synergy between the cathodes, electrolytes, and Na metal anodes. For example, high-capacity cathodes are essential for Na metal batteries. However, the parasitic reaction and O_2 crossover problem caused by the oxygen cathodes in Na-O_2 batteries and the polysulfide shuttle problem in Na-S battery seriously affect the overall performance of the Na metal-based full cells. Meanwhile, solvents, salts, and additives of electrolytes determine the composition in SEI. Therefore, the performance of Na metal batteries can be improved by adjusting the composition of electrolytes as well. From the perspective of energy density, more efficient battery systems should be designed to reduce unnecessary resource waste, such as lean-electrolyte batteries and batteries with less/free Na metal. In addition, to achieve the practical application of Na metal batteries as soon as possible, it is necessary to evaluate the performance of the anode in the pouch cells.

In conclusion, although there is still a long way to achieve high-performance Na metal anodes, the research of Na metal anodes has become one of the hottest topics in recent years. In addition, the relatively mature studies of Li metal anodes can provide effective guidance for the development of Na metal anodes, both in terms of the characterization and protection strategies. Therefore, we believe that with continuous efforts, Na metal anodes will have significant breakthroughs in the near future and act an important role in the next generation of large-scale energy storage applications.

Acknowledgements

J. X. acknowledges financial supports from the National Natural Science Foundation of China (No. 52002358), high-level talent internationalization training project of Henan province, and scientific and technological activities of Henan Province for scholars with overseas study experience (No. 002004025). G. X. W. and B. S. would like to thank the support of the Australian Research Council (ARC) through the ARC Discovery Project (No. DP210101389) and ARC Future Fellowship (No. FT220100561).

Funding note: Open Access funding enabled and organized by CAUL and its Member Institutions.

References

[1] Chen, Y.; Wang, T. Y.; Tian, H. J.; Su, D. W.; Zhang, Q.; Wang, G. X. Advances in lithium-sulfur batteries: From academic research to commercial viability. *Adv. Mater.* **2021**, *33*, 2003666.

[2] Lu, J.; Chen, Z. W.; Pan, F.; Cui, Y.; Amine, K. High-performance anode materials for rechargeable lithium-ion batteries. *Electrochem. Energy Rev.* **2018**, *1*, 35–53.

[3] He, X.; Bresser, D.; Passerini, S.; Baakes, F.; Krewer, U.; Lopez, J.; Mallia, C. T.; Shao-Horn, Y.; Cekic-Laskovic, I.; Wiemers-Meyer, S. et al. The passivity of lithium electrodes in liquid electrolytes for secondary batteries. *Nat. Rev. Mater.* **2021**, *6*, 1036–1052.

[4] Larcher, D.; Tarascon, J. M. Towards greener and more sustainable batteries for electrical energy storage. *Nat. Chem.* **2015**, *7*, 19–29.

[5] Blomgren, G. E. The development and future of lithium ion batteries. *J. Electrochem. Soc.* **2017**, *164*, A5019–A5025.

[6] Cano, Z. P.; Banham, D.; Ye, S. Y.; Hintennach, A.; Lu, J.; Fowler, M.; Chen, Z. W. Batteries and fuel cells for emerging electric vehicle markets. *Nat. Energy* **2018**, *3*, 279–289.

[7] Shen, X.; Zhang, X. Q.; Ding, F.; Huang, J. Q.; Xu, R.; Chen, X.; Yan, C.; Su, F. Y.; Chen, C. M.; Liu, X. J. et al. Advanced electrode materials in lithium batteries: Retrospect and prospect. *Energy Mater. Adv.* **2021**, *2021*, 1205324.

[8] Li, X. R.; Su, H. P.; Ma, C.; Hou, K. M.; Wang, J.; Lin, H. Z.; Shang, Y. Z.; Liu, H. L. Optimizations of graphitic carbon/silicon hybrids for scalable preparation with high-performance lithium-ion storage. *ACS Sustainable Chem. Eng.* **2022**, *10*, 5590–5598.

[9] Elia, G. A.; Ulissi, U.; Jeong, S.; Passerini, S.; Hassoun, J. Exceptional long-life performance of lithium-ion batteries using ionic liquid-based electrolytes. *Energy Environ. Sci.* **2016**, *9*, 3210–3220.

[10] Luo, Z.; Qiu, X. J.; Liu, C.; Li, S.; Wang, C. W.; Zou, G. Q.; Hou, H. S.; Ji, X. B. Interfacial challenges towards stable Li metal anode. *Nano Energy* **2021**, *79*, 105507.

[11] Xiang, J. W.; Yang, L. Y.; Yuan, L. X.; Yuan, K.; Zhang, Y.; Huang, Y. Y.; Lin, J.; Pan, F.; Huang, Y. H. Alkali-metal anodes: From lab to market. *Joule* **2019**, *3*, 2334–2363.

[12] Lin, L.; Zhang, C. K.; Huang, Y. Z.; Zhuang, Y. P.; Fan, M. J.; Lin, J.; Wang, L. S.; Xie, Q. S.; Peng, D. L. Challenge and strategies in room temperature sodium-sulfur batteries: A comparison with lithium-sulfur batteries. *Small* **2022**, *18*, 2107368.

[13] Lee, B.; Paek, E.; Mitlin, D.; Lee, S. W. Sodium metal anodes: Emerging solutions to dendrite growth. *Chem. Rev.* **2019**, *119*, 5416–5460.

[14] Hao, H. C.; Hutter, T.; Boyce, B. L.; Watt, J.; Liu, P. C.; Mitlin, D. Review of multifunctional separators: Stabilizing the cathode and the anode for alkali (Li, Na, and K) metal-sulfur and selenium batteries. *Chem. Rev.* **2022**, *122*, 8053–8125.

[15] Hwang, J. Y.; Myung, S. T.; Sun, Y. K. Recent progress in rechargeable potassium batteries. *Adv. Funct. Mater.* **2018**, *28*, 1802938.

[16] Zhao, Y.; Adair, K. R.; Sun, X. L. Recent developments and insights into the understanding of Na metal anodes for Na-metal batteries. *Energy Environ. Sci.* **2018**, *11*, 2673–2695.

[17] Chi, S. S.; Qi, X. G.; Hu, Y. S.; Fan, L. Z. 3D flexible carbon felt host for highly stable sodium metal anodes. *Adv. Energy Mater.* **2018**, *8*, 1702764.

[18] Wang, H.; Matios, E.; Luo, J. M.; Li, W. Y. Combining theories and experiments to understand the sodium nucleation behavior towards safe sodium metal batteries. *Chem. Soc. Rev.* **2020**, *49*, 3783–3805.

[19] Chu, C. X.; Li, R.; Cai, F. P.; Bai, Z. C.; Wang, Y. X.; Xu, X.; Wang, N. N.; Yang, J.; Dou, S. X. Recent advanced skeletons in sodium metal anodes. *Energy Environ. Sci.* **2021**, *14*, 4318–4340.

[20] Luo, W.; Zhang, Y.; Xu, S. M.; Dai, J. Q.; Hitz, E.; Li, Y. J.; Yang, C. P.; Chen, C. J.; Liu, B. Y.; Hu, L. B. Encapsulation of metallic Na in an electrically conductive host with porous channels as a highly stable Na metal anode. *Nano Lett.* **2017**, *17*, 3792–3797.

[21] Ruiz-Martínez, D.; Kovacs, A.; Gómez, R. Development of novel inorganic electrolytes for room temperature rechargeable sodium metal batteries. *Energy Environ. Sci.* **2017**, *10*, 1936–1941.

[22] Zheng, J. M.; Chen, S. R.; Zhao, W. G.; Song, J. H.; Engelhard, M. H.; Zhang, J. G. Extremely stable sodium metal batteries enabled by localized high-concentration electrolytes. *ACS Energy Lett.* **2018**, *3*, 315–321.

[23] Zeng, Z. Q.; Jiang, X. Y.; Li, R.; Yuan, D. D.; Ai, X. P.; Yang, H. X.; Cao, Y. L. A safer sodium-ion battery based on nonflammable organic phosphate electrolyte. *Adv. Sci.* **2016**, *3*, 1600066.

[24] Xu, R.; Cheng, X. B.; Yan, C.; Zhang, X. Q.; Xiao, Y.; Zhao, C. Z.; Huang, J. Q.; Zhang, Q. Artificial interphases for highly stable lithium metal anode. *Matter* **2019**, *1*, 317–344.

[25] Yan, C.; Cheng, X. B.; Tian, Y.; Chen, X.; Zhang, X. Q.; Li, W. J.; Huang, J. Q.; Zhang, Q. Dual-layered film protected lithium metal anode to enable dendrite-free lithium deposition. *Adv. Mater.* **2018**, *30*, 1707629.

[26] Guo, X. F.; Yang, Z.; Zhu, Y. F.; Liu, X. H.; He, X. X.; Li, L.; Qiao, Y.; Chou, S. L. High-voltage, highly reversible sodium batteries enabled by fluorine-rich electrode/electrolyte interphases. *Small Methods* **2022**, *6*, 2200209.

[27] Zhang, J.; Zhang, G. X.; Chen, Z. S.; Dai, H. L.; Hu, Q. M.; Liao, S. J.; Sun, S. H. Emerging applications of atomic layer deposition for lithium-sulfur and sodium-sulfur batteries. *Energy Storage Mater.* **2020**, *26*, 513–533.

[28] Yu, F.; Du, L.; Zhang, G. X.; Su, F. M.; Wang, W. C.; Sun, S. H. Electrode engineering by atomic layer deposition for sodium-ion batteries: From traditional to advanced batteries. *Adv. Funct. Mater.* **2020**, *30*, 1906890.

[29] Wang, T.; Hua, Y. B.; Xu, Z. W.; Yu, J. S. Recent advanced development of artificial interphase engineering for stable sodium metal anodes. *Small* **2022**, *18*, 2102250.

[30] Zhang, Y.; Wang, C. W.; Pastel, G.; Kuang, Y. D.; Xie, H.; Li, Y. J.; Liu, B. Y.; Luo, W.; Chen, C. J.; Hu, L. B. 3D wettable framework for dendrite-free alkali metal anodes. *Adv. Energy Mater.* **2018**, *8*, 1800635.

[31] Zhao, Y.; Yang, X. F.; Kuo, L. Y.; Kaghazchi, P.; Sun, Q.; Liang, J. N.; Wang, B. Q.; Lushington, A.; Li, R. Y.; Zhang, H. M. et al. High capacity, dendrite-free growth, and minimum volume change Na metal anode. *Small* **2018**, *14*, 1703717.

[32] Xu, Y. L.; Menon, A. S.; Harks, P. P. R. M. L.; Hermes, D. C.; Haverkate, L. A.; Unnikrishnan, S.; Mulder, F. M. Honeycomb-like porous 3D nickel electrodeposition for stable Li and Na metal anodes. *Energy Storage Mater.* **2018**, *12*, 69–78.

[33] Li, Z. P.; Zhu, K. J.; Liu, P.; Jiao, L. F. 3D confinement strategy for dendrite-free sodium metal batteries. *Adv. Energy Mater.* **2022**, *12*, 2100359.

[34] Zheng, X. Y.; Gu, Z. Y.; Fu, J.; Wang, H. T.; Ye, X. L.; Huang, L. Q.; Liu, X. Y.; Wu, X. L.; Luo, W.; Huang, Y. H. Knocking down the kinetic barriers towards fast-charging and low-temperature sodium metal batteries. *Energy Environ. Sci.* **2021**, *14*, 4936–4947.

[35] Ma, L. B.; Cui, J.; Yao, S. S.; Liu, X. M.; Luo, Y. S.; Shen, X. P.; Kim, J. K. Dendrite-free lithium metal and sodium metal batteries. *Energy Storage Mater.* **2020**, *27*, 522–554.

[36] Jäckle, M.; Groß, A. Microscopic properties of lithium, sodium, and magnesium battery anode materials related to possible dendrite growth. *J. Chem. Phys.* **2014**, *141*, 174710.

[37] Xiong, W. S.; Xia, Y.; Jiang, Y.; Qi, Y.; Sun, W. W.; He, D.; Liu, Y. M.; Zhao, X. Z. Highly conductive and robust three-dimensional host with excellent alkali metal infiltration boosts ultrastable lithium and sodium metal anodes. *ACS Appl. Mater. Interfaces* **2018**, *10*, 21254–21261.

[38] Tian, H. Z.; Seh, Z. W.; Yan, K.; Fu, Z. H.; Tang, P.; Lu, Y. Y.; Zhang, R. F.; Legut, D.; Cui, Y.; Zhang, Q. F. Theoretical investigation of 2D layered materials as protective films for lithium and sodium metal anodes. *Adv. Energy Mater.* **2017**, *7*, 1602528.

[39] Wang, J.; Zhang, J.; Cheng, S.; Yang, J.; Xi, Y. L.; Hou, X. G.; Xiao, Q. B.; Lin, H. Z. Long-life dendrite-free lithium metal electrode achieved by constructing a single metal atom anchored in a diffusion modulator layer. *Nano Lett.* **2021**, *21*, 3245–3253.

[40] Wang, J.; Jia, L. J.; Duan, S. R.; Liu, H. T.; Xiao, Q. B.; Li, T.; Fan, H. Y.; Feng, K.; Yang, J.; Wang, Q. et al. Single atomic cobalt catalyst significantly accelerates lithium ion diffusion in high mass loading Li_2S cathode. *Energy Storage Mater.* **2020**, *28*, 375–382.

[41] Liu, H.; Cheng, X. B.; Jin, Z. H.; Zhang, R.; Wang, G. X.; Chen, L. Q.; Liu, Q. B.; Huang, J. Q.; Zhang, Q. Recent advances in understanding dendrite growth on alkali metal anodes. *EnergyChem* **2019**, *1*, 100003.

[42] Bao, C. Y.; Wang, B.; Liu, P.; Wu, H.; Zhou, Y.; Wang, D. L.; Liu, H. K.; Dou, S. X. Solid electrolyte interphases on sodium metal anodes. *Adv. Funct. Mater.* **2020**, *30*, 2004891.

[43] Liu, W.; Liu, P. C.; Mitlin, D. Review of emerging concepts in SEI

analysis and artificial SEI membranes for lithium, sodium, and potassium metal battery anodes. *Adv. Energy Mater.* **2020**, *10*, 2002297.

[44] Ding, J. F.; Xu, R.; Yan, C.; Li, B. Q.; Yuan, H.; Huang, J. Q. A review on the failure and regulation of solid electrolyte interphase in lithium batteries. *J. Energy Chem.* **2021**, *59*, 306–319.

[45] Wang, Q. D.; Zhao, C. L.; Lv, X. H.; Lu, Y. X.; Lin, K.; Zhang, S. Q.; Kang, F. Y.; Hu, Y. S.; Li, B. H. Stabilizing a sodium-metal battery with the synergy effects of a sodiophilic matrix and fluorine-rich interface. *J. Mater. Chem. A* **2019**, *7*, 24857–24867.

[46] Cui, C. Y.; Yang, C. Y.; Eidson, N.; Chen, J.; Han, F. D.; Chen, L.; Luo, C.; Wang, P. F.; Fan, X. L.; Wang, C. S. A highly reversible, dendrite-free lithium metal anode enabled by a lithium-fluoride-enriched interphase. *Adv. Mater.* **2020**, *32*, 1906427.

[47] Hou, L. P.; Yao, N.; Xie, J.; Shi, P.; Sun, S. Y.; Jin, C. B.; Chen, C. M.; Liu, Q. B.; Li, B. Q.; Zhang, X. Q. et al. Modification of nitrate ion enables stable solid electrolyte interphase in lithium metal batteries. *Angew. Chem., Int. Ed.* **2022**, *61*, e202201406.

[48] Gao, Y.; Hou, Z.; Zhou, R.; Wang, D. N.; Guo, X. Y.; Zhu, Y.; Zhang, B. A. Critical roles of mechanical properties of solid electrolyte interphase for potassium metal anodes. *Adv. Funct. Mater.* **2022**, *32*, 2112399.

[49] Xu, M. Y.; Li, Y.; Ihsan-Ul-Haq, M.; Mubarak, N.; Liu, Z. J.; Wu, J. X.; Luo, Z. T.; Kim, J. K. NaF-rich solid electrolyte interphase for dendrite-free sodium metal batteries. *Energy Storage Mater.* **2022**, *44*, 477–486.

[50] Yu, Q. P.; Lu, Q. W.; Qi, X. G.; Zhao, S. Y.; He, Y. B.; Liu, L. L.; Li, J.; Zhou, D.; Hu, Y. S.; Yang, Q. H. et al. Liquid electrolyte immobilized in compact polymer matrix for stable sodium metal anodes. *Energy Storage Mater.* **2019**, *23*, 610–616.

[51] Seh, Z. W.; Sun, J.; Sun, Y. M.; Cui, Y. A highly reversible room-temperature sodium metal anode. *ACS Cent. Sci.* **2015**, *1*, 449–455.

[52] Cao, R. G.; Mishra, K.; Li, X. L.; Qian, J. F.; Engelhard, M. H.; Bowden, M. E.; Han, K. S.; Mueller, K. T.; Henderson, W. A.; Zhang, J. G. Enabling room temperature sodium metal batteries. *Nano Energy* **2016**, *30*, 825–830.

[53] Schafzahl, L.; Hanzu, I.; Wilkening, M.; Freunberger, S. A. An electrolyte for reversible cycling of sodium metal and intercalation compounds. *ChemSusChem* **2017**, *10*, 401–408.

[54] Zheng, X. Y.; Gu, Z. Y.; Liu, X. Y.; Wang, Z. Q.; Wen, J. Y.; Wu, X. L.; Luo, W.; Huang, Y. H. Bridging the immiscibility of an all-fluoride fire extinguishant with highly-fluorinated electrolytes toward safe sodium metal batteries. *Energy Environ. Sci.* **2020**, *13*, 1788–1798.

[55] Zhou, X. Z.; Zhang, Q.; Zhu, Z.; Cai, Y. C.; Li, H. X.; Li, F. J. Anion-reinforced solvation for a gradient inorganic-rich interphase enables high-rate and stable sodium batteries. *Angew. Chem., Int. Ed.* **2022**, *61*, e202205045.

[56] Chen, X.; Shen, X.; Hou, T. Z.; Zhang, R.; Peng, H. J.; Zhang, Q. Ion-solvent chemistry-inspired cation-additive strategy to stabilize electrolytes for sodium-metal batteries. *Chem* **2020**, *6*, 2242–2256.

[57] Zhou, J.; Wang, Y. Y.; Wang, J. W.; Liu, Y.; Li, Y. M.; Cheng, L. W.; Ding, Y.; Dong, S.; Zhu, Q. N.; Tang, M. Y. et al. Low-temperature and high-rate sodium metal batteries enabled by electrolyte chemistry. *Energy Storage Mater.* **2022**, *50*, 47–54.

[58] Wang, H. P.; Zhu, C. L.; Liu, J. D.; Qi, S. H.; Wu, M. G.; Huang, J. D.; Wu, D. X.; Ma, J. M. Formation of NaF-rich solid electrolyte interphase on Na anode through additive-induced anion-enriched structure of Na^+ solvation. *Angew. Chem., Int. Ed.* **2022**, *61*, e202208506.

[59] Rakov, D. A.; Chen, F. F.; Ferdousi, S. A.; Li, H.; Pathirana, T.; Simonov, A. N.; Howlett, P. C.; Atkin, R.; Forsyth, M. Engineering high-energy-density sodium battery anodes for improved cycling with superconcentrated ionic-liquid electrolytes. *Nat. Mater.* **2020**, *19*, 1096–1101.

[60] Choudhury, S.; Wei, S. Y.; Ozhabes, Y.; Gunceler, D.; Zachman, M. J.; Tu, Z. Y.; Shin, J. H.; Nath, P.; Agrawal, A.; Kourkoutis, L. F. et al. Designing solid–liquid interphases for sodium batteries. *Nat. Commun.* **2017**, *8*, 898.

[61] Tian, H. J.; Shao, H. Z.; Chen, Y.; Fang, X. Q.; Xiong, P.; Sun, B.; Notten, P. H. L.; Wang, G. X. Ultra-stable sodium metal-iodine batteries enabled by an *in-situ* solid electrolyte interphase. *Nano Energy* **2019**, *57*, 692–702.

[62] Shi, P. C.; Zhang, S. P.; Lu, G. X.; Wang, L. F.; Jiang, Y.; Liu, F. F.; Yao, Y.; Yang, H.; Ma, M. Z.; Ye, S. F. et al. Red phosphorous-derived protective layers with high ionic conductivity and mechanical strength on dendrite-free sodium and potassium metal anodes. *Adv. Energy Mater.* **2021**, *11*, 2003381.

[63] Luo, Z.; Tao, S. S.; Tian, Y.; Xu, L. Q.; Wang, Y.; Cao, X. Y.; Wang, Y. P.; Deng, W. T.; Zou, G. Q.; Liu, H. et al. Robust artificial interlayer for columnar sodium metal anode. *Nano Energy* **2022**, *97*, 107203.

[64] Kim, J.; Kim, J.; Jeong, J.; Park, J.; Park, C. Y.; Park, S.; Lim, S. G.; Lee, K. T.; Choi, N. S.; Byon, H. R. et al. Designing fluorine-free electrolytes for stable sodium metal anodes and high-power seawater batteries via SEI reconstruction. *Energy Environ. Sci.* **2022**, *15*, 4109–4118.

[65] Luo, W.; Lin, C. F.; Zhao, O.; Noked, M.; Zhang, Y.; Rubloff, G. W.; Hu, L. B. Ultrathin surface coating enables the stable sodium metal anode. *Adv. Energy Mater.* **2017**, *7*, 1601526.

[66] Jiang, F. Y.; Li, T. J.; Ju, P.; Sun, J. C.; Liu, C.; Li, Y. W.; Sun, X. Q.; Chen, C. C. Nano-SiO_2 coating enabled uniform Na stripping/plating for dendrite-free and long-life sodium metal batteries. *Nanoscale Adv.* **2019**, *1*, 4989–4994.

[67] Che, H. Y.; Chen, S. L.; Xie, Y. Y.; Wang, H.; Amine, K.; Liao, X. Z.; Ma, Z. F. Electrolyte design strategies and research progress for room-temperature sodium-ion batteries. *Energy Environ. Sci.* **2017**, *10*, 1075–1101.

[68] Tikekar, M. D.; Archer, L. A.; Koch, D. L. Stability analysis of electrodeposition across a structured electrolyte with immobilized anions. *J. Electrochem. Soc.* **2014**, *161*, A847–A855.

[69] Wei, S. Y.; Choudhury, S.; Xu, J.; Nath, P.; Tu, Z. Y.; Archer, L. A. Highly stable sodium batteries enabled by functional ionic polymer membranes. *Adv. Mater.* **2017**, *29*, 1605512.

[70] Wu, Y. X.; Li, Y.; Wang, Y.; Liu, Q.; Chen, Q. G.; Chen, M. H. Advances and prospects of PVDF based polymer electrolytes. *J. Energy Chem.* **2022**, *64*, 62–84.

[71] Li, L. G.; Wang, M. C.; Wang, J.; Ye, F. M.; Wang, S. F.; Xu, Y. N.; Liu, J. Y.; Xu, G. G.; Zhang, Y.; Zhang, Y. Y. et al. Asymmetric gel polymer electrolyte with high lithium ion conductivity for dendrite-free lithium metal batteries. *J. Mater. Chem. A* **2020**, *8*, 8033–8040.

[72] Hou, Z.; Wang, W. H.; Yu, Y. K.; Zhao, X. X.; Chen, Q. W.; Zhao, L. F.; Di, Q.; Ju, H. X.; Quan, Z. W. Poly(vinylidene difluoride) coating on Cu current collector for high-performance Na metal anode. *Energy Storage Mater.* **2020**, *24*, 588–593.

[73] Zhu, M.; Wang, G. Y.; Liu, X.; Guo, B. K.; Xu, G.; Huang, Z. Y.; Wu, M. H.; Liu, H. K.; Dou, S. X.; Wu, C. Dendrite-free sodium metal anodes enabled by a sodium benzenedithiolate-rich protection layer. *Angew. Chem., Int. Ed.* **2020**, *59*, 6596–6600.

[74] Zhu, M.; Zhang, Y. J.; Yu, F. F.; Huang, Z. Y.; Zhang, Y.; Li, L. L.; Wang, G. Y.; Wen, L. Y.; Liu, H. K.; Dou, S. X. et al. Stable sodium metal anode enabled by an interface protection layer rich in organic sulfide salt. *Nano Lett.* **2021**, *21*, 619–627.

[75] Lu, Q. Q.; Omar, A.; Ding, L.; Oswald, S.; Hantusch, M.; Giebeler, L.; Nielsch, K.; Mikhailova, D. A facile method to stabilize sodium metal anodes towards high-performance sodium batteries. *J. Mater. Chem. A* **2021**, *9*, 9038–9047.

[76] Liu, K.; Pei, A.; Lee, H. R.; Kong, B.; Liu, N.; Lin, D. C.; Liu, Y. Y.; Liu, C.; Hsu, P. C.; Bao, Z. N. et al. Lithium metal anodes with an adaptive "solid–liquid" interfacial protective layer. *J. Am. Chem. Soc.* **2017**, *139*, 4815–4820.

[77] Luo, J.; Fang, C. C.; Wu, N. L. High polarity poly(vinylidene difluoride) thin coating for dendrite-free and high-performance lithium metal anodes. *Adv. Energy Mater.* **2018**, *8*, 1701482.

[78] Wang, C. X.; Fu, X. W.; Lin, S. N.; Liu, J.; Zhong, W. H. A protein-enabled protective film with functions of self-adapting and anion-anchoring for stabilizing lithium-metal batteries. *J. Energy Chem.* **2022**, *64*, 485–495.

[79] Xu, R.; Zhang, X. Q.; Cheng, X. B.; Peng, H. J.; Zhao, C. Z.; Yan, C.; Huang, J. Q. Artificial soft-rigid protective layer for dendrite-free lithium metal anode. *Adv. Funct. Mater.* **2018**, *28*, 1705838.

[80] Wang, S. Y.; Chen, Y. W.; Jie, Y. L.; Lang, S. Y.; Song, J. H.; Lei, Z. W.; Wang, S.; Ren, X. D.; Wang, D.; Li, X. L. et al. Stable sodium metal batteries via manipulation of electrolyte solvation structure. *Small Methods* **2020**, *4*, 1900856.
[81] Zhao, Y.; Zheng, K.; Sun, X. L. Addressing interfacial issues in liquid-based and solid-state batteries by atomic and molecular layer deposition. *Joule* **2018**, *2*, 2583–2604.
[82] Zhao, Y.; Goncharova, L. V.; Sun, Q.; Li, X.; Lushington, A.; Wang, B. Q.; Li, R. Y.; Dai, F.; Cai, M.; Sun, X. L. Robust metallic lithium anode protection by the molecular-layer-deposition technique. *Small Methods* **2018**, *2*, 1700417.
[83] Zhao, Y.; Goncharova, L. V.; Zhang, Q.; Kaghazchi, P.; Sun, Q.; Lushington, A.; Wang, B. Q.; Li, R. Y.; Sun, X. L. Inorganic-organic coating via molecular layer deposition enables long life sodium metal anode. *Nano Lett.* **2017**, *17*, 5653–5659.
[84] Zhang, S. M.; Zhao, Y.; Zhao, F. P.; Zhang, L.; Wang, C. H.; Li, X. N.; Liang, J. W.; Li, W. H.; Sun, Q.; Yu, C. et al. Gradiently sodiated alucone as an interfacial stabilizing strategy for solid-state Na metal batteries. *Adv. Funct. Mater.* **2020**, *30*, 2001118.
[85] Lin, X. T.; Sun, Y. P.; Sun, Q.; Luo, J.; Zhao, Y.; Zhao, C. T.; Yang, X. F.; Wang, C. H.; Huo, H. Y.; Li, R. Y. et al. Reviving anode protection layer in Na-O_2 batteries: Failure mechanism and resolving strategy. *Adv. Energy Mater.* **2021**, *11*, 2003789.
[86] Kang, Q.; Li, Y.; Zhuang, Z. C.; Wang, D. S.; Zhi, C. Y.; Jiang, P. K.; Huang, X. Y. Dielectric polymer based electrolytes for high-performance all-solid-state lithium metal batteries. *J. Energy Chem.* **2022**, *69*, 194–204.
[87] Kim, Y. J.; Lee, H.; Noh, H.; Lee, J.; Kim, S.; Ryou, M. H.; Lee, Y. M.; Kim, H. T. Enhancing the cycling stability of sodium metal electrodes by building an inorganic-organic composite protective layer. *ACS Appl. Mater. Interfaces* **2017**, *9*, 6000–6006.
[88] Chen, Q. W.; Hou, Z.; Sun, Z. Z.; Pu, Y. Y.; Jiang, Y. B.; Zhao, Y.; He, H.; Zhang, T. X.; Huang, L. M. Polymer-inorganic composite protective layer for stable Na metal anodes. *ACS Appl. Energy Mater.* **2020**, *3*, 2900–2906.
[89] Wang, S. Y.; Jie, Y. L.; Sun, Z. H.; Cai, W. B.; Chen, Y. W.; Huang, F. Y.; Liu, Y.; Li, X. P.; Du, R. Q.; Cao, R. G. et al. An implantable artificial protective layer enables stable sodium metal anodes. *ACS Appl. Energy Mater.* **2020**, *3*, 8688–8694.
[90] Zhang, J. L.; Wang, S.; Wang, W. H.; Li, B. H. Stabilizing sodium metal anode through facile construction of organic–metal interface. *J. Energy Chem.* **2022**, *66*, 133–139.
[91] Xia, X. M.; Du, C. F.; Zhong, S. E.; Jiang, Y.; Yu, H.; Sun, W. P.; Pan, H. G.; Rui, X. H.; Yu, Y. Homogeneous Na deposition enabling high-energy Na-metal batteries. *Adv. Funct. Mater.* **2022**, *32*, 2110280.
[92] Xu, J.; Lawson, T.; Fan, H. B.; Su, D. W.; Wang, G. X. Updated metal compounds (MOFs, –S, –OH, –N, –C) used as cathode materials for lithium-sulfur batteries. *Adv. Energy Mater.* **2018**, *8*, 1702607.
[93] Qian, J.; Li, Y.; Zhang, M. L.; Luo, R.; Wang, F. J.; Ye, Y. S.; Xing, Y.; Li, W. L.; Qu, W. J.; Wang, L. L. et al. Protecting lithium/sodium metal anode with metal-organic framework based compact and robust shield. *Nano Energy* **2019**, *60*, 866–874.
[94] Li, H. H.; Zhang, H.; Wu, F. L.; Zarrabeitia, M.; Geiger, D.; Kaiser, U.; Varzi, A.; Passerini, S. Sodiophilic current collectors based on MOF-derived nanocomposites for anode-less Na-metal batteries. *Adv. Energy Mater.* **2022**, *12*, 2202293.
[95] Liu, D. Z.; Li, Z.; Li, X.; Chen, X.; Li, Z.; Yuan, L. X.; Huang, Y. H. Stable room-temperature sodium-sulfur batteries in ether-based electrolytes enabled by the fluoroethylene carbonate additive. *ACS Appl. Mater. Interfaces* **2022**, *14*, 6658–6666.
[96] Aurbach, D.; Markevich, E.; Salitra, G. High energy density rechargeable batteries based on Li metal anodes. The role of unique surface chemistry developed in solutions containing fluorinated organic co-solvents. *J. Am. Chem. Soc.* **2021**, *143*, 21161–21176.
[97] Lee, Y.; Lee, J.; Lee, J.; Kim, K.; Cha, A. M.; Kang, S. J.; Wi, T.; Kang, S. J.; Lee, H. W.; Choi, N. S. Fluoroethylene carbonate-based electrolyte with 1 M sodium bis(fluorosulfonyl)imide enables high-performance sodium metal electrodes. *ACS Appl. Mater. Interfaces* **2018**, *10*, 15270–15280.
[98] Li, Y. Q.; Yang, Y.; Lu, Y. X.; Zhou, Q.; Qi, X. G.; Meng, Q. S.; Rong, X. H.; Chen, L. Q.; Hu, Y. S. Ultralow-concentration electrolyte for Na-ion batteries. *ACS Energy Lett.* **2020**, *5*, 1156–1158.
[99] Jiang, R.; Hong, L.; Liu, Y. C.; Wang, Y. D.; Patel, S.; Feng, X. Y.; Xiang, H. F. An acetamide additive stabilizing ultra-low concentration electrolyte for long-cycling and high-rate sodium metal battery. *Energy Storage Mater.* **2021**, *42*, 370–379.
[100] Zhu, M.; Li, L. L.; Zhang, Y. J.; Wu, K.; Yu, F. F.; Huang, Z. Y.; Wang, G. Y.; Li, J. Y.; Wen, L. Y.; Liu, H. K. et al. An *in-situ* formed stable interface layer for high-performance sodium metal anode in a non-flammable electrolyte. *Energy Storage Mater.* **2021**, *42*, 145–153.
[101] Wei, S. Y.; Xu, S. M.; Agrawral, A.; Choudhury, S.; Lu, Y. Y.; Tu, Z. Y.; Ma, L.; Archer, L. A. A stable room-temperature sodium-sulfur battery. *Nat. Commun.* **2016**, *7*, 11722.
[102] Li, R. T.; Du, Y. X.; Li, Y. H.; He, Z. X.; Dai, L.; Wang, L.; Wu, X. W.; Zhang, J. J.; Yi, J. Alloying strategy for high-performance zinc metal anodes. *ACS Energy Lett.* **2023**, *8*, 457–476.
[103] Ding, F.; Xu, W.; Graff, G. L.; Zhang, J.; Sushko, M. L.; Chen, X. L.; Shao, Y. Y.; Engelhard, M. H.; Nie, Z. M.; Xiao, J. et al. Dendrite-free lithium deposition via self-healing electrostatic shield mechanism. *J. Am. Chem. Soc.* **2013**, *135*, 4450–4456.
[104] Chen, J. W.; Peng, Y.; Yin, Y.; Liu, M. Z.; Fang, Z.; Xie, Y. H.; Chen, B. W.; Cao, Y. J.; Xing, L. D.; Huang, J. H. et al. High energy density Na-metal batteries enabled by a tailored carbonate-based electrolyte. *Energy Environ. Sci.* **2022**, *15*, 3360–3368.
[105] Zhou, B. X.; Bonakdarpour, A.; Stoševski, I.; Fang, B. Z.; Wilkinson, D. P. Modification of Cu current collectors for lithium metal batteries—A review. *Prog. Mater. Sci.* **2022**, *130*, 100996.
[106] Zhang, C.; Lv, W.; Zhou, G. M.; Huang, Z. J.; Zhang, Y. B.; Lyu, R. Y.; Wu, H. L.; Yun, Q. B.; Kang, F. Y.; Yang, Q. H. Vertically aligned lithiophilic CuO nanosheets on a Cu collector to stabilize lithium deposition for lithium metal batteries. *Adv. Energy Mater.* **2018**, *8*, 1703404.
[107] Wang, C. L.; Wang, H.; Matios, E.; Hu, X. F.; Li, W. Y. A chemically engineered porous copper matrix with cylindrical core–shell skeleton as a stable host for metallic sodium anodes. *Adv. Funct. Mater.* **2018**, *28*, 1802282.
[108] Liu, S.; Tang, S.; Zhang, X. Y.; Wang, A. X.; Yang, Q. H.; Luo, J. Y. Porous Al current collector for dendrite-free Na metal anodes. *Nano Lett.* **2017**, *17*, 5862–5868.
[109] Li, S. Y.; Liu, Q. L.; Zhou, J. J.; Pan, T.; Gao, L. N.; Zhang, W. D.; Fan, L.; Lu, Y. Y. Hierarchical Co_3O_4 nanofiber-carbon sheet skeleton with superior Na/Li-philic property enabling highly stable alkali metal batteries. *Adv. Funct. Mater.* **2019**, *29*, 1808847.
[110] Wang, Z. H.; Zhang, X. L.; Zhou, S. Y.; Edstrom, K.; Strømme, M.; Nyholm, L. Lightweight, thin, and flexible silver nanopaper electrodes for high-capacity dendrite-free sodium metal anodes. *Adv. Funct. Mater.* **2018**, *28*, 1804038.
[111] Yang, W.; Yang, W.; Dong, L. B.; Shao, G. J.; Wang, G. X.; Peng, X. W. Hierarchical ZnO nanorod arrays grown on copper foam as an advanced three-dimensional skeleton for dendrite-free sodium metal anodes. *Nano Energy* **2021**, *80*, 105563.
[112] Liu, F. F.; Wang, L. F.; Ling, F. X.; Zhou, X. F.; Jiang, Y.; Yao, Y.; Yang, H.; Shao, Y.; Wu, X. J.; Rui, X. H. et al. Homogeneous metallic deposition regulated by porous framework and selenization interphase toward stable sodium/potassium anodes. *Adv. Funct. Mater.* **2022**, *32*, 2210166.
[113] Chen, Q. L.; Liu, B.; Zhang, L.; Xie, Q. S.; Zhang, Y. G.; Lin, J.; Qu, B. H.; Wang, L. S.; Sa, B. S.; Peng, D. L. Sodiophilic Zn/SnO_2 porous scaffold to stabilize sodium deposition for sodium metal batteries. *Chem. Eng. J.* **2021**, *404*, 126469.
[114] Lu, X.; Luo, J. M.; Matios, E.; Zhang, Y. W.; Wang, H.; Hu, X. F.; Wang, C. L.; Wang, H. K.; Wang, J. Y.; Li, W. Y. Enabling high-performance sodium metal anodes via a sodiophilic structure constructed by hierarchical Sb_2MoO_6 microspheres. *Nano Energy* **2020**, *69*, 104446.
[115] Zheng, X. Y.; Yang, W. J.; Wang, Z. Q.; Huang, L. Q.; Geng, S.; Wen, J. Y.; Luo, W.; Huang, Y. H. Embedding a percolated dual-conductive skeleton with high sodiophilicity toward stable sodium metal anodes. *Nano Energy* **2020**, *69*, 104387.

[116] Wang, Y. X.; Dong, H.; Katyal, N.; Hao, H. C.; Liu, P. C.; Celio, H.; Henkelman, G.; Watt, J.; Mitlin, D. A sodium-antimony-telluride intermetallic allows sodium-metal cycling at 100% depth of discharge and as an anode-free metal battery. *Adv. Mater.* **2022**, *34*, 2106005.

[117] Jin, Q. Z.; Lu, H. F.; Zhang, Z. L.; Xu, J.; Sun, B.; Jin, Y.; Jiang, K. Synergistic manipulation of Na^+ flux and surface-preferred effect enabling high-areal-capacity and dendrite-free sodium metal battery. *Adv. Sci. (Weinh.)* **2022**, *9*, 2103845.

[118] Deng, W.; Zhou, X. F.; Fang, Q. L.; Liu, Z. P. Microscale lithium metal stored inside cellular graphene scaffold toward advanced metallic lithium anodes. *Adv. Energy Mater.* **2018**, *8*, 1703152.

[119] Wang, A. X.; Hu, X. F.; Tang, H. Q.; Zhang, C. Y.; Liu, S.; Yang, Y. W.; Yang, Q. H.; Luo, J. Y. Processable and moldable sodium-metal anodes. *Angew. Chem., Int. Ed.* **2017**, *56*, 11921–11926.

[120] Sun, B.; Li, P.; Zhang, J. Q.; Wang, D.; Munroe, P.; Wang, C. Y.; Notten, P. H. L.; Wang, G. X. Dendrite-free sodium-metal anodes for high-energy sodium-metal batteries. *Adv. Mater.* **2018**, *30*, 1801334.

[121] Liu, L.; Yin, Y. X.; Li, J. Y.; Li, N. W.; Zeng, X. X.; Ye, H.; Guo, Y. G.; Wan, L. J. Free-standing hollow carbon fibers as high-capacity containers for stable lithium metal anodes. *Joule* **2017**, *1*, 563–575.

[122] Cao, Q. H.; Gao, H.; Gao, Y.; Yang, J.; Li, C.; Pu, J.; Du, J. J.; Yang, J. Y.; Cai, D. M.; Pan, Z. H. et al. Regulating dendrite-free zinc deposition by 3D zincopilic nitrogen-doped vertical graphene for high-performance flexible Zn-ion batteries. *Adv. Funct. Mater.* **2021**, *31*, 2103922.

[123] Xu, Z.; Guo, Z. Y.; Madhu, R.; Xie, F.; Chen, R. X.; Wang, J.; Tebyetekerwa, M.; Hu, Y. S.; Titirici, M. M. Homogenous metallic deposition regulated by defect-rich skeletons for sodium metal batteries. *Energy Environ. Sci.* **2021**, *14*, 6381–6393.

[124] Yang, S. J.; Xu, S. S.; Tong, J. Y.; Ding, D. H.; Wang, G.; Chen, R. Z.; Jin, P. K.; Wang, X. C. Overlooked role of nitrogen dopant in carbon catalysts for peroxymonosulfate activation: Intrinsic defects or extrinsic defects. *Appl. Catal. B: Environ.* **2021**, *295*, 120291.

[125] Mubarak, N.; Rehman, F.; Ihsan-Ul-Haq, M.; Xu, M. Y.; Li, Y.; Zhao, Y. H.; Luo, Z. T.; Huang, B. L.; Kim, J. K. Highly sodiophilic, defect-rich, lignin-derived skeletal carbon nanofiber host for sodium metal batteries. *Adv. Energy Mater.* **2022**, *12*, 2103904.

[126] Tao, L.; Hu, A. Y.; Mu, L. Q.; Kautz, D. J.; Xu, Z. R.; Feng, Y. M.; Huang, H. B.; Lin, F. A self-sodiophilic carbon host promotes the cyclability of sodium anode. *Adv. Funct. Mater.* **2021**, *31*, 2007556.

[127] Li, T. J.; Sun, J. C.; Gao, S. Z.; Xiao, B.; Cheng, J. B.; Zhou, Y. L.; Sun, X. Q.; Jiang, F. Y.; Yan, Z. H.; Xiong, S. L. Superior sodium metal anodes enabled by sodiophilic carbonized coconut framework with 3D tubular structure. *Adv. Energy Mater.* **2021**, *11*, 2003699.

[128] Liu, B.; Lei, D. N.; Wang, J.; Zhang, Q. F.; Zhang, Y. G.; He, W.; Zheng, H. F.; Sa, B. S.; Xie, Q. S.; Peng, D. L. et al. 3D uniform nitrogen-doped carbon skeleton for ultra-stable sodium metal anode. *Nano Res.* **2020**, *13*, 2136–2142.

[129] Geng, M. N.; Han, D. M.; Huang, Z. H.; Wang, S. J.; Xiao, M.; Zhang, S. C.; Sun, L. Y.; Huang, S.; Meng, Y. Z. A stable anode-free Na-S full cell at room temperature. *Energy Storage Mater.* **2022**, *52*, 230–237.

[130] Liu, P.; Yi, H. T.; Zheng, S. Y.; Li, Z. P.; Zhu, K. J.; Sun, Z. Q.; Jin, T.; Jiao, L. F. Regulating deposition behavior of sodium ions for dendrite-free sodium-metal anode. *Adv. Energy Mater.* **2021**, *11*, 2101976.

[131] Cui, X. Y.; Wang, Y. J.; Wu, H. D.; Lin, X. D.; Tang, S.; Xu, P.; Liao, H. G.; Zheng, M. S.; Dong, Q. F. A carbon foam with sodiophilic surface for highly reversible, ultra-long cycle sodium metal anode. *Adv. Sci.* **2021**, *8*, 2003178.

[132] Zheng, X. Y.; Li, P.; Cao, Z.; Luo, W.; Sun, F. Z.; Wang, Z. Q.; Ding, B.; Wang, G. X.; Huang, Y. H. Boosting the reversibility of sodium metal anode via heteroatom-doped hollow carbon fibers. *Small* **2019**, *15*, 1902688.

[133] Xiao, J.; Xiao, N.; Li, K.; Zhang, L. P.; Ma, X. Q.; Li, Y.; Leng, C. Y.; Qiu, J. S. Sodium metal anodes with self-correction function based on fluorine-superdoped CNTs/cellulose nanofibrils composite paper. *Adv. Funct. Mater.* **2022**, *32*, 2111133.

[134] Wang, H.; Matios, E.; Wang, C. L.; Luo, J. M.; Lu, X.; Hu, X. F.; Zhang, Y. W.; Li, W. Y. Tin nanoparticles embedded in a carbon buffer layer as preferential nucleation sites for stable sodium metal anodes. *J. Mater. Chem. A* **2019**, *7*, 23747–23755.

[135] Yue, L.; Qi, Y. R.; Niu, Y. B.; Bao, S. J.; Xu, M. W. Low-barrier, dendrite-free, and stable Na plating/stripping enabled by gradient sodiophilic carbon skeleton. *Adv. Energy Mater.* **2021**, *11*, 2102497.

[136] Wu, J. X.; Zou, P. C.; Ihsan-Ul-Haq, M.; Mubarak, N.; Susca, A.; Li, B. H.; Ciucci, F.; Kim, J. K. Sodiophilically graded gold coating on carbon skeletons for highly stable sodium metal anodes. *Small* **2020**, *16*, 2003815.

[137] Sun, Z. W.; Jin, H. C.; Ye, Y. D.; Xie, H. Y.; Jia, W. S.; Jin, S.; Ji, H. X. Guiding sodium deposition through a sodiophobic–sodiophilic gradient interfacial layer for highly stable sodium metal anodes. *ACS Appl. Energy Mater.* **2021**, *4*, 2724–2731.

[138] Xu, Y.; Wang, C. L.; Matios, E.; Luo, J. M.; Hu, X. F.; Yue, Q.; Kang, Y. J.; Li, W. Y. Sodium deposition with a controlled location and orientation for dendrite-free sodium metal batteries. *Adv. Energy Mater.* **2020**, *10*, 2002308.

[139] Zhang, Z. G.; Li, L.; Zhu, Z. C.; Fan, Y. T.; Lin, X. P.; Gu, Y. F.; He, S.; Li, Q. H. Homogenous sdiophilic MoS_2/nitrogen-doped carbon nanofibers to stabilize sodium deposition for sodium metal batteries. *Energy Storage Mater.* **2022**, *53*, 363–370.

[140] Li, Z.; Wang, C. L.; Ling, F. X.; Wang, L. F.; Bai, R. L.; Shao, Y.; Chen, Q. W.; Yuan, H.; Yu, Y.; Tan, Y. Q. Room-temperature sodium-sulfur batteries: Rules for catalyst selection and electrode design. *Adv. Mater.* **2022**, *34*, 2204214.

[141] Lai, X. J.; Xu, Z. M.; Yang, X. F.; Ke, Q. J.; Xu, Q. S.; Wang, Z. S.; Lu, Y. Y.; Qiu, Y. C. Long cycle Life and high-rate sodium metal batteries enabled by regulating 3D frameworks with artificial solid-state interphases. *Adv. Energy Mater.* **2022**, *12*, 2103540.

[142] Zhuang, Y. P.; Deng, D. Y.; Lin, L.; Liu, B.; Qu, S. S.; Li, S. C.; Zhang, Y. G.; Sa, B. S.; Wang, L. S.; Wei, Q. L. et al. Ion-conductive gradient sodiophilic 3D scaffold induced homogeneous sodium deposition for highly stable sodium metal batteries. *Nano Energy* **2022**, *97*, 107202.

[143] Ma, L. B.; Luo, D.; Li, Y. T.; Chen, X.; Wu, K. L.; Xu, J.; Cao, Y. J.; Luo, M. C.; Manke, I.; Lai, F. L. et al. Architecture design of MXene-based materials for sodium-chemistry based batteries. *Nano Energy* **2022**, *101*, 107590.

[144] He, X.; Jin, S.; Miao, L. C.; Cai, Y. C.; Hou, Y. P.; Li, H. X.; Zhang, K.; Yan, Z. H.; Chen, J. A 3D hydroxylated MXene/carbon nanotubes composite as a scaffold for dendrite-free sodium-metal electrodes. *Angew. Chem., Int. Ed.* **2020**, *59*, 16705–16711.

[145] Luo, J. M.; Wang, C. L.; Wang, H.; Hu, X. F.; Matios, E.; Lu, X.; Zhang, W. K.; Tao, X. Y.; Li, W. Y. Pillared MXene with ultralarge interlayer spacing as a stable matrix for high performance sodium metal anodes. *Adv. Funct. Mater.* **2019**, *29*, 1805946.

[146] Bao, C. Y.; Wang, J. H.; Wang, B.; Sun, J. G.; He, L. C.; Pan, Z. H.; Jiang, Y. P.; Wang, D. L.; Liu, X. M.; Dou, S. X. et al. 3D sodiophilic Ti_3C_2 MXene@g-C_3N_4 hetero-interphase raises the stability of sodium metal anodes. *ACS Nano* **2022**, *16*, 17197–17209.

[147] Ma, P.; Fang, D. L.; Liu, Y. L.; Shang, Y.; Shi, Y. M.; Yang, H. Y. MXene-based materials for electrochemical sodium-ion storage. *Adv. Sci.* **2021**, *8*, 2003185.

[148] Fang, Y. Z.; Lian, R. Q.; Li, H. P.; Zhang, Y.; Gong, Z.; Zhu, K.; Ye, K.; Yan, J.; Wang, G. L.; Gao, Y. et al. Induction of planar sodium growth on MXene ($Ti_3C_2T_x$)-modified carbon cloth hosts for flexible sodium metal anodes. *ACS Nano* **2020**, *14*, 8744–8753.

[149] Luo, J. M.; Lu, X.; Matios, E.; Wang, C. L.; Wang, H.; Zhang, Y. W.; Hu, X. F.; Li, W. Y. Tunable MXene-derived 1D/2D hybrid nanoarchitectures as a stable matrix for dendrite-free and ultrahigh capacity sodium metal anode. *Nano Lett.* **2020**, *20*, 7700–7708.

[150] Wang, S. Y.; Liu, Y.; Lu, K.; Cai, W. B.; Jie, Y. L.; Huang, F. Y.; Li, X. P.; Cao, R. G.; Jiao, S. H. Engineering rGO/MXene hybrid film as an anode host for stable sodium-metal batteries. *Energy Fuels* **2021**, *35*, 4587–4595.

[151] He, X.; Ni, Y. X.; Li, Y. X.; Sun, H. X.; Lu, Y.; Li, H. X.; Yan, Z.

H.; Zhang, K.; Chen, J. An MXene-based metal anode with stepped sodiophilic gradient structure enables a large current density for rechargeable Na-O_2 batteries. *Adv. Mater.* **2022**, *34*, 2106565.

[152] Wang, Z. X.; Huang, Z. X.; Wang, H.; Li, W. D.; Wang, B. Y.; Xu, J. M.; Xu, T. T.; Zang, J. H.; Kong, D. Z.; Li, X. J. et al. 3D-printed sodiophilic V_2CT_x/rGO-CNT MXene microgrid aerogel for stable Na metal anode with high areal capacity. *ACS Nano* **2022**, *16*, 9105–9116.

[153] Bai, M.; Tang, X. Y.; Liu, S. Y.; Wang, H. L.; Liu, Y. J.; Shao, A. H.; Zhang, M.; Wang, Z. Q.; Ma, Y. An anodeless, mechanically flexible and energy/power dense sodium battery prototype. *Energy Environ. Sci.* **2022**, *15*, 4686–4699.

[154] Zhao, Q.; Stalin, S.; Archer, L. A. Stabilizing metal battery anodes through the design of solid electrolyte interphases. *Joule* **2021**, *5*, 1119–1142.

[155] Liu, H.; Cheng, X. B.; Huang, J. Q.; Kaskel, S.; Chou, S. L.; Park, H. S.; Zhang, Q. Alloy anodes for rechargeable alkali-metal batteries: Progress and challenge. *ACS Mater. Lett.* **2019**, *1*, 217–229.

[156] Jhang, L. J.; Wang, D. W.; Silver, A.; Li, X. L.; Reed, D.; Wang, D. H. Stable all-solid-state sodium-sulfur batteries for low-temperature operation enabled by sodium alloy anode and confined sulfur cathode. *Nano Energy* **2023**, *105*, 107995.

[157] Choudhury, S.; Tu, Z. Y.; Stalin, S.; Vu, D.; Fawole, K.; Gunceler, D.; Sundararaman, R.; Archer, L. A. Electroless formation of hybrid lithium anodes for fast interfacial ion transport. *Angew. Chem., Int. Ed.* **2017**, *56*, 13070–13077.

[158] Tang, S.; Qiu, Z.; Wang, X. Y.; Gu, Y.; Zhang, X. G.; Wang, W. W.; Yan, J. W.; Zheng, M. S.; Dong, Q. F.; Mao, B. W. A room-temperature sodium metal anode enabled by a sodiophilic layer. *Nano Energy* **2018**, *48*, 101–106.

[159] Tu, Z. Y.; Choudhury, S.; Zachman, M. J.; Wei, S. Y.; Zhang, K. H.; Kourkoutis, L. F.; Archer, L. A. Fast ion transport at solid–solid interfaces in hybrid battery anodes. *Nat. Energy* **2018**, *3*, 310–316.

[160] Xu, Z. X.; Yang, J.; Zhang, T.; Sun, L. M.; Nuli, Y.; Wang, J. L.; Hirano, S. I. Stable Na metal anode enabled by a reinforced multistructural SEI layer. *Adv. Funct. Mater.* **2019**, *29*, 1901924.

[161] Kumar, V.; Eng, A. Y. S.; Wang, Y.; Nguyen, D. T.; Ng, M. F.; Seh, Z. W. An artificial metal-alloy interphase for high-rate and long-life sodium-sulfur batteries. *Energy Storage Mater.* **2020**, *29*, 1–8.

[162] Wang, L.; Shang, J.; Huang, Q. Y.; Hu, H.; Zhang, Y. Q.; Xie, C.; Luo, Y. F.; Gao, Y.; Wang, H. X.; Zheng, Z. J. Smoothing the sodium-metal anode with a self-regulating alloy interface for high-energy and sustainable sodium-metal batteries. *Adv. Mater.* **2021**, *33*, 2102802.

[163] Deng, Y.; Zheng, J. X.; Zhao, Q.; Yin, J. D.; Biswal, P.; Hibi, Y.; Jin, S.; Archer, L. A. Highly reversible sodium metal battery anodes via alloying heterointerfaces. *Small* **2022**, *18*, 2203409.

[164] Wang, H. W.; Gu, X. K.; Zheng, X. S.; Pan, H. B.; Zhu, J. F.; Chen, S.; Cao, L. N.; Li, W. X.; Lu, J. L. Disentangling the size-dependent geometric and electronic effects of palladium nanocatalysts beyond selectivity. *Sci. Adv.* **2019**, *5*, eaat6413.

[165] Hu, X. F.; Matios, E.; Zhang, Y. W.; Wang, C. L.; Luo, J. M.; Li, W. Y. Enabling stable sodium metal cycling by sodiophilic interphase in a polymer electrolyte system. *J. Energy Chem.* **2021**, *63*, 305–311.

[166] Tang, S.; Zhang, Y. Y.; Zhang, X. G.; Li, J. T.; Wang, X. Y.; Yan, J. W.; Wu, D. Y.; Zheng, M. S.; Dong, Q. F.; Mao, B. W. Stable Na plating and stripping electrochemistry promoted by *in situ* construction of an alloy-based sodiophilic interphase. *Adv. Mater.* **2019**, *31*, 1807495.

[167] Jiang, Y.; Yang, Y.; Ling, F. X.; Lu, G. X.; Huang, F. Y.; Tao, X. Y.; Wu, S. F.; Cheng, X. L.; Liu, F. F.; Li, D. J. et al. Artificial heterogeneous interphase layer with boosted ion affinity and diffusion for Na/K-metal batteries. *Adv. Mater.* **2022**, *34*, 2109439.

[168] Xia, X. M.; Xu, S. T.; Tang, F.; Yao, Y.; Wang, L. F.; Liu, L.; He, S. N.; Yang, Y. X.; Sun, W. P.; Xu, C. et al. A multifunctional interphase layer enabling superior sodium-metal batteries under ambient temperature and −40 °C. *Adv. Mater.* **2023**, *35*, 2209511.

[169] Jin, X.; Zhao, Y.; Shen, Z. H.; Pu, J.; Xu, X. X.; Zhong, C. L.; Zhang, S.; Li, J. C.; Zhang, H. G. Interfacial design principle of sodiophilicity-regulated interlayer deposition in a sandwiched sodium metal anode. *Energy Storage Mater.* **2020**, *31*, 221–229.

[170] Wang, G. Y.; Zhang, Y.; Guo, B. K.; Tang, L.; Xu, G.; Zhang, Y. J.; Wu, M. H.; Liu, H. K.; Dou, S. X.; Wu, C. Core–shell C@Sb nanoparticles as a nucleation layer for high-performance sodium metal anodes. *Nano Lett.* **2020**, *20*, 4464–4471.

[171] Xie, Y. Y.; Hu, J. X.; Han, Z. X.; Wang, T. S.; Zheng, J. Q.; Gan, L.; Lai, Y. Q.; Zhang, Z. A. Encapsulating sodium deposition into carbon rhombic dodecahedron guided by sodiophilic sites for dendrite-free Na metal batteries. *Energy Storage Mater.* **2020**, *30*, 1–8.

[172] Lee, K.; Lee, Y. J.; Lee, M. J.; Han, J.; Lim, J.; Ryu, K.; Yoon, H.; Kim, B. H.; Kim, B. J.; Lee, S. W. A 3D hierarchical host with enhanced sodiophilicity enabling anode-free sodium-metal batteries. *Adv. Mater.* **2022**, *34*, 2109767.

[173] Wang, G. Y.; Yu, F. F.; Zhang, Y.; Zhang, Y. J.; Zhu, M.; Xu, G.; Wu, M. H.; Liu, H. K.; Dou, S. X.; Wu, C. 2D Sn/C freestanding frameworks as a robust nucleation layer for highly stable sodium metal anodes with a high utilization. *Nano Energy* **2021**, *79*, 105457.

[174] Xu, Y.; Matios, E.; Luo, J. M.; Li, T.; Lu, X.; Jiang, S. H.; Yue, Q.; Li, W. Y.; Kang, Y. J. SnO_2 quantum dots enabled site-directed sodium deposition for stable sodium metal batteries. *Nano Lett.* **2021**, *21*, 816–822.

[175] Zhao, L. F.; Hu, Z.; Huang, Z. Y.; Tao, Y.; Lai, W. H.; Zhao, A. L.; Liu, Q. N.; Peng, J.; Lei, Y. J.; Wang, Y. X. et al. *In situ* plating of Mg sodiophilic seeds and evolving sodium fluoride protective layers for superior sodium metal anodes. *Adv. Energy Mater.* **2022**, *12*, 2200990.

[176] Bai, M.; Zhang, K. R.; Du, D.; Tang, X. Y.; Liu, Y. J.; Wang, H. L.; Zhang, M.; Liu, S. Y.; Ma, Y. SnSb binary alloy induced heterogeneous nucleation within the confined nanospace: Toward dendrite-free, flexible and energy/power dense sodium metal batteries. *Energy Storage Mater.* **2021**, *42*, 219–230.

[177] Zhai, P. B.; Wang, T. S.; Yang, W. W.; Cui, S. Q.; Zhang, P.; Nie, A. M.; Zhang, Q. F.; Gong, Y. J. Uniform lithium deposition assisted by single-atom doping toward high-performance lithium metal anodes. *Adv. Energy Mater.* **2019**, *9*, 1804019.

[178] Wang, A. Q.; Li, J.; Zhang, T. Heterogeneous single-atom catalysis. *Nat. Rev. Chem.* **2018**, *2*, 65–81.

[179] Zhang, J.; You, C. Y.; Lin, H. Z.; Wang, J. Electrochemical kinetic modulators in lithium-sulfur batteries: From defect-rich catalysts to single atomic catalysts. *Energy Environ. Mater.* **2022**, *5*, 731–750.

[180] Wang, J.; Jia, L. J.; Zhong, J.; Xiao, Q. B.; Wang, C.; Zang, K. T.; Liu, H. T.; Zheng, H. C.; Luo, J.; Yang, J. et al. Single-atom catalyst boosts electrochemical conversion reactions in batteries. *Energy Storage Mater.* **2019**, *18*, 246–252.

[181] Yang, T. Z.; Qian, T.; Sun, Y. W.; Zhong, J.; Rosei, F.; Yan, C. L. Mega high utilization of sodium metal anodes enabled by single zinc atom sites. *Nano Lett.* **2019**, *19*, 7827–7835.

[182] Hu, X. F.; Joo, P. H.; Wang, H.; Matios, E.; Wang, C. L.; Luo, J. M.; Lu, X.; Yang, K. S.; Li, W. Y. Nip the sodium dendrites in the bud on planar doped graphene in liquid/gel electrolytes. *Adv. Funct. Mater.* **2019**, *29*, 1807974.

[183] Li, Y. J.; Xu, P.; Mou, J. R.; Xue, S. F.; Huang, S. M.; Hu, J. H.; Dong, Q. F.; Yang, C. H.; Liu, M. L. Single cobalt atoms decorated N-doped carbon polyhedron enabled dendrite-free sodium metal anode. *Small Methods* **2021**, *5*, 2100833.

[184] Zhang, E. H.; Hu, X.; Meng, L. Z.; Qiu, M.; Chen, J. X.; Liu, Y. J.; Liu, G. Y.; Zhuang, Z. C.; Zheng, X. B.; Zheng, L. R. et al. Single-atom yttrium engineering Janus electrode for rechargeable Na-S batteries. *J. Am. Chem. Soc.* **2022**, *144*, 18995–19007.

[185] Li, X.; Ye, W. B.; Xu, P.; Huang, H. H.; Fan, J. M.; Yuan, R. M.; Zheng, M. S.; Wang, M. S.; Dong, Q. F. An encapsulation-based sodium storage via Zn-single-atom implanted carbon nanotubes. *Adv. Mater.* **2022**, *34*, 2202898.